AD-A068 464 ARMY ARMAMENT RESEARCH AND DEVELOPMENT COMMAND ABERD--ETC F/G 21/8.2
RESPONSE OF A ROCKET MOTOR TO TRANSVERSE BLAST LOADING.(U)
FEB 79 N J HUFFINGTON, H L WISNIEWSKI

UNCLASSIFIED ARBRL-TR-02144 SBIE-AD-E430 215 NL

1 OF 1
AD A068464

END
DATE FILMED
6 -79
DDC

(12) LEVEL III

AD-E430215

TECHNICAL REPORT ARBRL-TR-02144

RESPONSE OF A ROCKET MOTOR TO TRANSVERSE BLAST LOADING

Norris J. Huffington, Jr.
Henry L. Wisniewski

February 1979

US ARMY ARMAMENT RESEARCH AND DEVELOPMENT COMMAND
BALLISTIC RESEARCH LABORATORY
ABERDEEN PROVING GROUND, MARYLAND

Destroy this report when it is no longer needed.
Do not return it to the originator.

Secondary distribution of this report by originating or sponsoring activity is prohibited.

Additional copies of this report may be obtained from the National Technical Information Service, U.S. Department of Commerce, Springfield, Virginia 22161.

The findings in this report are not to be construed as an official Department of the Army position, unless so designated by other authorized documents.

The use of trade names or manufacturers' names in this report does not constitute indorsement of any commercial product.

UNCLASSIFIED

SECURITY CLASSIFICATION OF THIS PAGE (When Data Entered)

REPORT DOCUMENTATION PAGE

READ INSTRUCTIONS BEFORE COMPLETING FORM

1. REPORT NUMBER: TECHNICAL REPORT ARBRL-TR-02144
2. GOVT ACCESSION NO.
3. RECIPIENT'S CATALOG NUMBER

4. TITLE (and Subtitle): RESPONSE OF A ROCKET MOTOR TO TRANSVERSE BLAST LOADING
5. TYPE OF REPORT & PERIOD COVERED: Final
6. PERFORMING ORG. REPORT NUMBER

7. AUTHOR(s): Norris J. Huffington, Jr.; Henry L. Wisniewski
8. CONTRACT OR GRANT NUMBER(s)

9. PERFORMING ORGANIZATION NAME AND ADDRESS: US Army Ballistic Research Laboratory (ATTN: DRDAR-BLT) Aberdeen Proving Ground, Maryland 21005
10. PROGRAM ELEMENT, PROJECT, TASK AREA & WORK UNIT NUMBERS: RDT&E 1L162618AH80; RDT&E 1W162118AH75

11. CONTROLLING OFFICE NAME AND ADDRESS: US Army Armament Research and Development Command; US Army Ballistic Research Laboratory (ATTN: DRDAR-BL) Aberdeen Proving Ground, Maryland 21005
12. REPORT DATE: FEBRUARY 1979
13. NUMBER OF PAGES: 53

14. MONITORING AGENCY NAME & ADDRESS (if different from Controlling Office)
15. SECURITY CLASS. (of this report): UNCLASSIFIED
15a. DECLASSIFICATION/DOWNGRADING SCHEDULE

16. DISTRIBUTION STATEMENT (of this Report)

Approved for public release; distribution unlimited.

17. DISTRIBUTION STATEMENT (of the abstract entered in Block 20, if different from Report)

18. SUPPLEMENTARY NOTES

19. KEY WORDS (Continue on reverse side if necessary and identify by block number)

Structural Response	Vulnerability Analysis
Rocket Motors	Internal Pressurization
Air Blast Loading	Finite Difference Method
Solid Propellant	Plane Strain
Elastoplastic Material	Modal Analysis

20. ABSTRACT (Continue on reverse side if necessary and identify by block number)

The effects of propellant inertia and of internal pressurization on the structural response of solid propellant rocket motors subjected to transverse air blast loading have been investigated, both analytically and numerically. The numerical predictions were accomplished using the BRL version of the PETROS 3.5 computer program, which employs the finite difference method to solve the equations governing finite amplitude elastoplastic response of thin shells. The response of a typical rocket motor configuration was calculated for the limiting situations of the bare motor case and of the motor case containing the

DD FORM 1 JAN 73 1473 EDITION OF 1 NOV 65 IS OBSOLETE

UNCLASSIFIED

SECURITY CLASSIFICATION OF THIS PAGE (When Data Entered)

complete propellant grain, each with no internal pressurization and with the pressurization resulting from propellant combustion. These calculations showed that the unpressurized motors experience a much larger deformation than the pressurized motors for the same blast loading. The most significant result is the quantification of the greater vulnerability of rocket motors prior to their ignition, whether on the launcher or as upper stages of in-flight missiles.

TABLE OF CONTENTS

I. INTRODUCTION

At the request of the U.S. Army Missile Research and Development Command and the Harry Diamond Laboratories the Ballistic Research Laboratory has undertaken the development of an appropriate methodology for assessing the vulnerability of solid rocket motors to lateral air blast loading, especially that produced by nuclear weapons detonation. It is desired that this methodology be compatible with analysis procedures currently used for design or evaluation of rocket motors, specifically:

(1) a finite element structural analysis code[1], AMG074, for operational loads analysis,

(2) a finite element stress wave analysis code[2], AMG063, for treating x-ray-induced stress waves,

(3) a photon energy deposition code[3], KNISH, for predicting energy absorption and subsequent stress wave loadings, and

(4) a computer program[4] for combined operational and nuclear effects loads which employs the three preceding codes.

To achieve this objective, a contract has been assigned to personnel familiar with the cited analysis procedures for the development of a two-dimensional plane strain analysis of the motor cross section, including the viscoelastic propellant grain, elastoplastic deformation of the motor case, effects of internal pressurization, operational loads plus side-on blast loading subsuming diffraction effects.

---

[1] *J. J. Brisbane, "Advances in Stress Analysis of Solid Propellant Rocket Grains", Rohm and Haas Company Technical Report S-268, Contract DAAH01-70-C-0152, September 1970.*

[2] *R. S. Dunham, "Dynamic Analysis of One Dimensional Thermorheologically Simple Viscoelastic Solids With Nonlinear Heat Conduction Analysis", U.S. Army Missile Command Report No. RK-TR-70-13, July 1970.*

[3] *J. Case et al, "The KNISH/AMGO Photon Energy Deposition and Viscoelastic Material Response Computer Program", Physics International Company, PITR-307-3, August 1972.*

[4] *T. L. Cost and G. E. Weeks, "Automated Evaluation of Interceptor Rocket Motor Designs Under Combined Operational and Nuclear Effects Loads", University of Alabama BER Report No. 176-97, July 1974.*

However, it was felt desirable to explore the utility of the BRL version of the PETROS 3.5 code[5] for predicting the response of rocket motors. This computer program, which is based on a nonlinear finite difference analysis, has been extensively employed to treat blast-induced response of thin elastoplastic shell structures. By contrast with the finite element analysis model to be produced by a contractor, the PETROS 3.5 model is valid for large deflections and can be employed to treat an entire rocket motor case rather than just a sectional cut. However, it has no provision for inclusion of the propellant grain in the calculations and rather extensive modifications to the code would be required to incorporate even plane strain deformation of the propellant. Consequently, in this report the PETROS 3.5 code will only be used to treat the plane strain response of a bare cylinder (motor case), which may in the future be compared with the contractor's finite element analysis, and the cylinder plus an approximate modeling of the mass effect of the propellant.

The representation employed for the blast loading includes both the diffraction and the drag phases of loading since both phases contribute to the response to nuclear blast. Nevertheless, the methodology is equally applicable for predicting response to blast from conventional weapons.

In addition to results of numerical analysis obtained with the PETROS 3.5 code, this report contains analytical solutions for the effect of pressurization upon the vibration characteristics of elastic cylinders and for the response of such cylinders to transverse blast loading. There is also a discussion of conditions under which solid propellant motors are most susceptible to blast-induced damage.

II. PLANE STRAIN CYLINDER RESPONSE CALCULATIONS

When resorting to numerical analysis one must naturally assign values to all parameters appearing in the formulation. The values selected below are not identified with any existing system but do fall within ranges of practical interest.

A. Rocket Motor Parameters

A representative solid propellant rocket motor cross section (see Figure 1) was selected for exercise of the PETROS 3.5 computer program in its plane strain option. In addition to the geometric data shown

---

[5] *S. D. Pirotin, B. A. Berg, and E. A. Witmer, "PETROS 3.5: New Developments and Program Manual for the Finite-Difference Calculation of Large Elastic-Plastic Transient Deformations of Multilayer Variable-Thickness Shells", U.S. Army Ballistic Research Laboratories Contract Report No. 211, February 1975.* (AD #A007215)

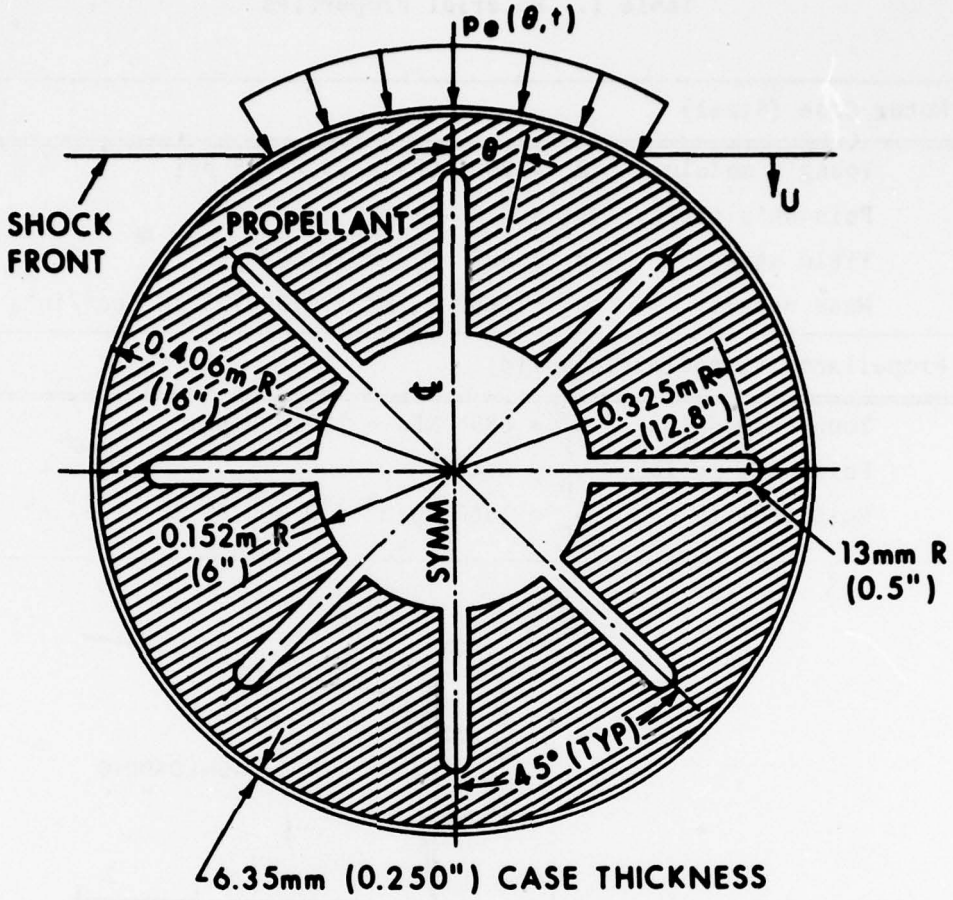

Figure 1. Rocket Motor Cross Section

on this Figure, the material property parameters listed in Table I were selected. The steel motor case was assumed to have the linear strain hardening uniaxial stress-strain characteristics shown in Figure 2 and to exhibit no strain-rate effects. Bi-axial plastic flow was analyzed using the von Mises yield criterion and the associated flow rule in accordance with the mechanical sublayer model[6]. Although the propellant is being modeled as a viscoelastic material in the cited finite element

[6] *L. Marino, J. W. Leech, and E. A. Witmer, "PETROS 2: A New Finite-Difference Method and Program for the Calculation of Large Elastic-Plastic Dynamically-Induced Deformations of General Thin Shells", U.S. Army Ballistic Research Laboratories Contract Report No. 12, December 1969.* (AD #708773)

Table I. Material Properties

Motor Case (Steel)		
Young's modulus	E_c = 200 GPa = 29 × 10^6 psi	
Poisson's ratio	ν_c = 0.3	
Yield stress	σ_o = 483 MPa = 70,000 psi	
Mass density	ρ_c = 7850 kg/m^3 = 0.000735 lb sec^2/in^4	
Propellant (Viscoelastic Solid)		
Young's modulus	E_p = 689 MPa = 100,000 psi	
Poisson's ratio	ν_p = 0.472	
Mass density	ρ_p = 1660 kg/m^3 = 0.000155 lb sec^2/in^4	

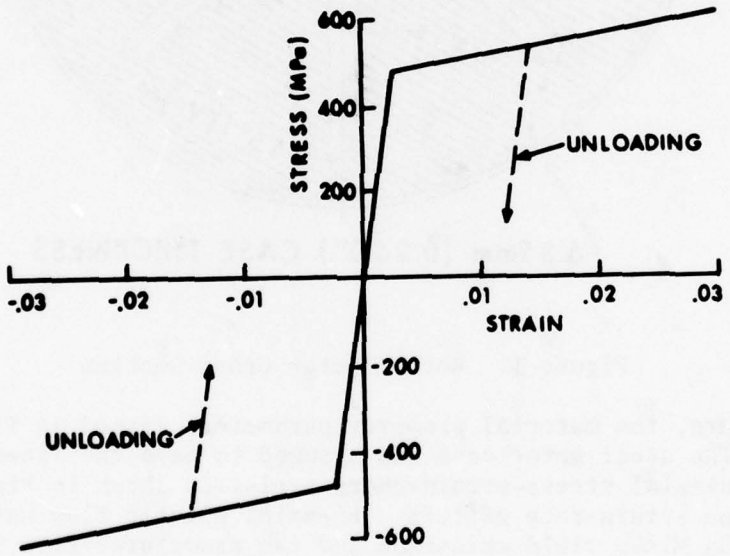

Figure 2. Postulated Uniaxial Stress-Strain Curve for Motor Case Material

analysis, the lumped mass treatment of the propellant in the PETROS 3.5 calculations required use of only the propellant density.

B. Blast Loading Model

The blast loading is introduced as a plane shock wave having an exponentially decaying tail, moving down from above as shown in Figure 1. Although surface overpressures $p_e(\theta,t)$ obtained experimentally or by refined hydrodynamic calculations can be readily introduced into the PETROS 3.5 code, it is convenient to employ the following functional representation for the blast loading which includes the essential aspects of wave reflection, diffraction, and post-envelopment drag loading:

$$p_e(\theta,t) = \begin{cases} 0 & \text{for } t < t_a \\ \left.\begin{cases} [p_r \cos\theta + p_s(1-\cos\theta)]e^{-\lambda(t-t_a)} & \text{for } -90° \leq \theta \leq 90° \\ p_s e^{-\lambda(t-t_a)} & \text{for } 90° < |\theta| \leq 180° \end{cases}\right\} & \text{for } t \geq t_a \end{cases} \tag{1}$$

where

p_o = ambient pressure

p_s = side-on overpressure of incident shock

p_r = reflected peak overpressure

a_o = sonic velocity at ambient conditions

U = shock front velocity

t_a = arrival time of shock front

R = outside radius of cylinder

λ = decay coefficient

and

$$p_r = 2p_s\left(\frac{7p_o + 4p_s}{7p_o + p_s}\right) \tag{2}$$

$$U = a_o\sqrt{1 + \frac{6p_s}{7p_o}} \tag{3}$$

$$t_a = \frac{R(1 - \cos\theta)}{U} \tag{4}$$

While response predictions have been made for several values of incident overpressure, the results which follow have been obtained for one level of blast loading, the parameters for which are listed in Table II.

Table II. Blast Wave Parameters

Parameter	SI Units	English Units
a_o	340 m/s	13400 in/sec
p_o	101 kPa	14.7 psi
p_s	79.3 kPa	11.5 psi
U	440 m/s	17300 in/sec
λ	4.35 s^{-1}	4.35 sec^{-1}
p_r	207 kPa	30.0 psi

The value of the decay coefficient λ was estimated from blast data curves[7] for a one kiloton nuclear weapon.

C. Internal Loading

In addition to response predictions using the foregoing external loading, which would correspond to the pre-ignition response for the rocket motor stage under consideration, calculations have also been performed for cases where the motor had an additional internal pressurization p_i (produced by propellant combustion) prior to this blast loading. For the most part the value p_i = 6.89 MPa (1000 psi) has been used for this internal pressure, although a limited study of the effect of varying this parameter will also be reported.

III. FINITE DIFFERENCE MODELING

A. Computational Grid

The finite difference grid employed for all the PETROS 3.5 calculations is shown in Figure 3. Since both the responding structure and the applied loads are symmetric with respect to the vertical plane,

[7] *S. Glasstone (Editor), "The Effects of Nuclear Weapons", United States Atomic Energy Commission, April 1962.*

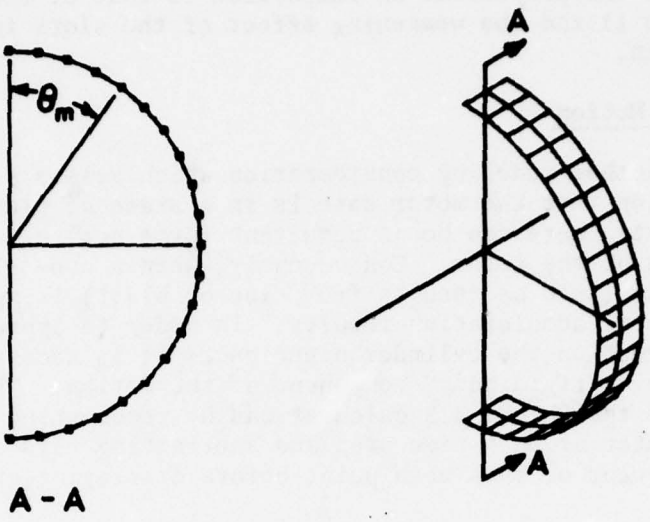

Figure 3. Finite Difference Grid

it is only necessary to model the response of one-half of the cylinder. Further, because there is no longitudinal variation of any quantities involved in a plane strain analysis there are only two independent variables, the angles θ and time, resulting in quite economical computer runs.

B. Propellant Mass Effect

In the finite difference equations of motion for the mesh point at θ_m (m = integer) the mass is that of the shell (motor case) lying between the radial planes at angles $(\theta_{m-1} + \theta_m)/2$ and $(\theta_m + \theta_{m+1})/2$. When it was desired to take account of the mass of the propellant in the response prediction the mass of propellant lying between the same two radial planes was added to the motor case mass at θ_m. Therefore, the effective mass will vary as a function of the discrete angles θ_m owing to the slots in the star pattern of the propellant grain (see Figure 1). It is recognized that this procedure provides a rather crude approximation to the propellant mass effect since many two-dimensional response modes are thereby inhibited. Nevertheless it appears to be the most rational procedure which does not entail extensive modification of the shell response code. The resistance of the propellant grain to deformation is also neglected in this modeling, an approximation which may not be too serious owing to the relatively

low strength of the propellant in comparison to that of the steel motor case (see Table I) and the weakening effect of the slots in the propellant grain.

C. Rigid Body Motion

There is another modeling consideration which arises as a consequence of the assumption that the motor case is in a state of plane strain. In this stress state there can be no resultant force acting tangential to a cross section of the motor. Consequently, when a non-self-equilibrating external loading (such as results from side-on blast) is applied to the cylinder a lateral acceleration results. In order to appreciate the extent of deformation the cylinder experiences it is necessary to subtract out this "rigid body" component of the motion. This was accomplished in the PETROS 3.5 calculations by recomputing the location of the mass center at each time step and subtracting this quantity from the position vector of each mesh point before displaying graphical results.

IV. NUMERICAL ANALYSIS RESULTS

A. Unpressurized Cylinders

In Figure 4 the undeformed cylinder cross section of the bare motor case is compared with that at 30 ms, which is approximately the time of maximum deflection. It should be emphasized that in this figure the

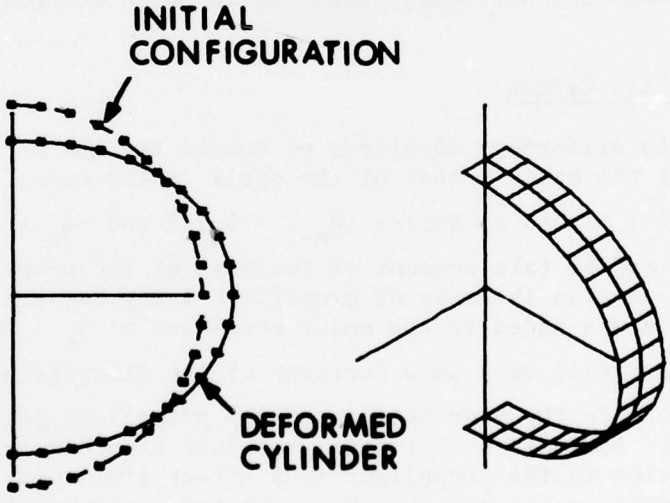

Figure 4. Deflection Pattern for Unpressurized Bare Cylinder

deflections are plotted to the same scale as the initial configuration; i.e., the deflections are large, entailing both nonlinear geometric effects and elastoplastic material behavior. The deflected cross section corresponds principally to the lowest frequency flexural mode for a ring or cylinder (the n = 2, s = 1 mode, see Chapter V.A.). The deflection responses of a point on the crown line ($\theta = 0°$) of cylinders having no internal pressurization are shown in Figure 5, for both the bare motor case and the motor configuration of Figure 1 (where the effect of propellant mass has been included as described above). As expected, the effect of the propellant is to reduce both the amplitude and frequency of the response.

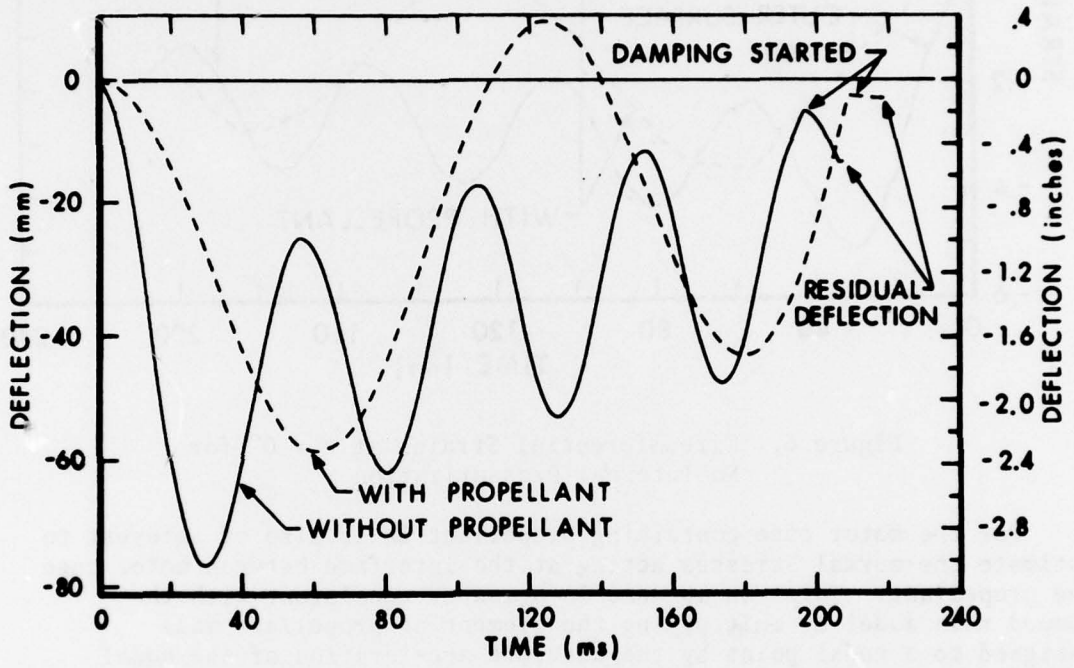

Figure 5. Deflections at $\theta = 0°$ for No Internal Pressurization

The predicted circumferential strains at the crown line are displayed in Figure 6. Since the curves for the inner and outer surfaces (of the motor case) are nearly symmetric with respect to the zero strain line it may be inferred that the response is mostly flexural, which is consistent with Figure 4. Similar strain variations were obtained at $\theta = 90°$ and $180°$. At 192 ms, by which time all plastic deformation had ceased, the external load was removed and an artificial damping was introduced to dissipate rapidly the remaining kinetic energy. In this manner it was possible to identify the values of residual deflection and residual strains indicated on Figures 5 and 6, respectively.

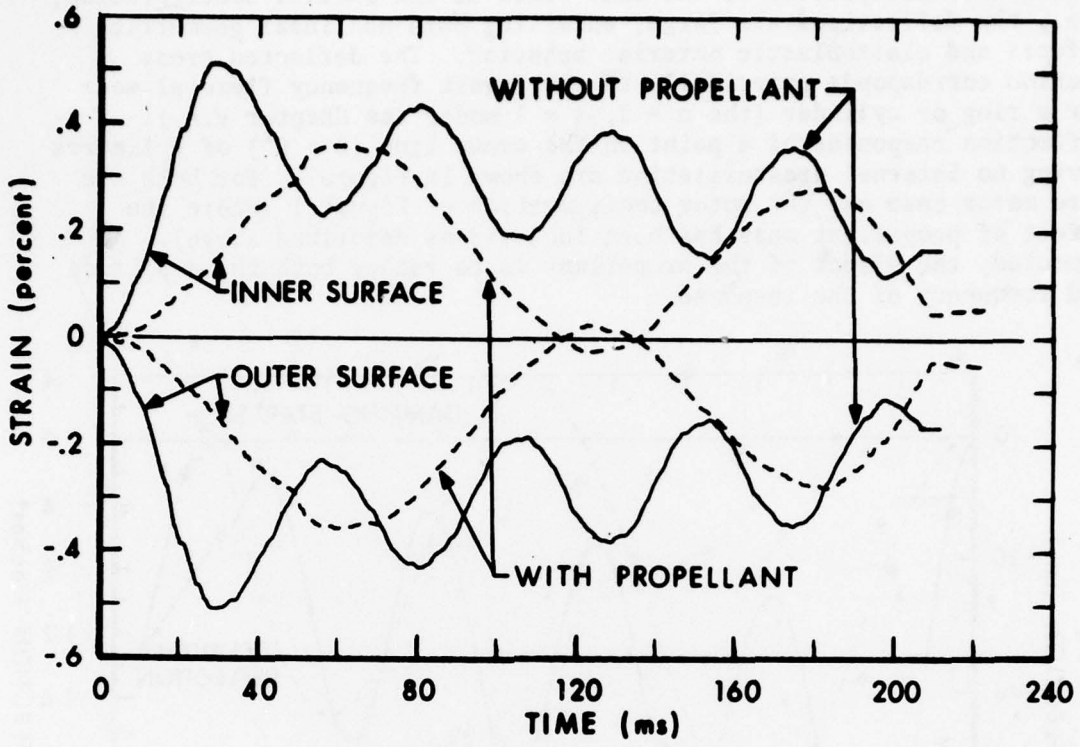

Figure 6. Circumferential Strains at $\theta = 0°$ for No Internal Pressurization

For the motor case containing propellant it is also of interest to estimate the normal stresses acting at the interface between motor case and propellant. This can be done in a manner consistent with the lumped mass model by multiplying the element of propellant mass assigned to a nodal point by the absolute acceleration of the nodal point and dividing by the appropriate interface surface area. The acceleration histories* of the nodal points at $\theta = 0°$ and $\theta = 180°$ are shown in Figures 7 and 8, respectively. Tensile interface stresses are

*The presence of high frequency oscillations in these plots may appear suspicious in view of the rather low frequency deflection response in Figure 5. However, relatively low amplitude extensional modes (the s = 2 family discussed in Chapter V) when amplified by the square of their large circular frequencies (as is effectively done when calculating accelerations) can become dominant in the manner shown in Figures 7 and 8. Love[8] remarks that such modes would probably be difficult to excite. It appears that diffracting a shock wave around a cylinder is quite effective in exciting these high frequency modes.

[8] A. E. H. Love, "A Treatise on the Mathematical Theory of Elasticity", Fourth Edition, Dover Publications, 1944, p. 454.

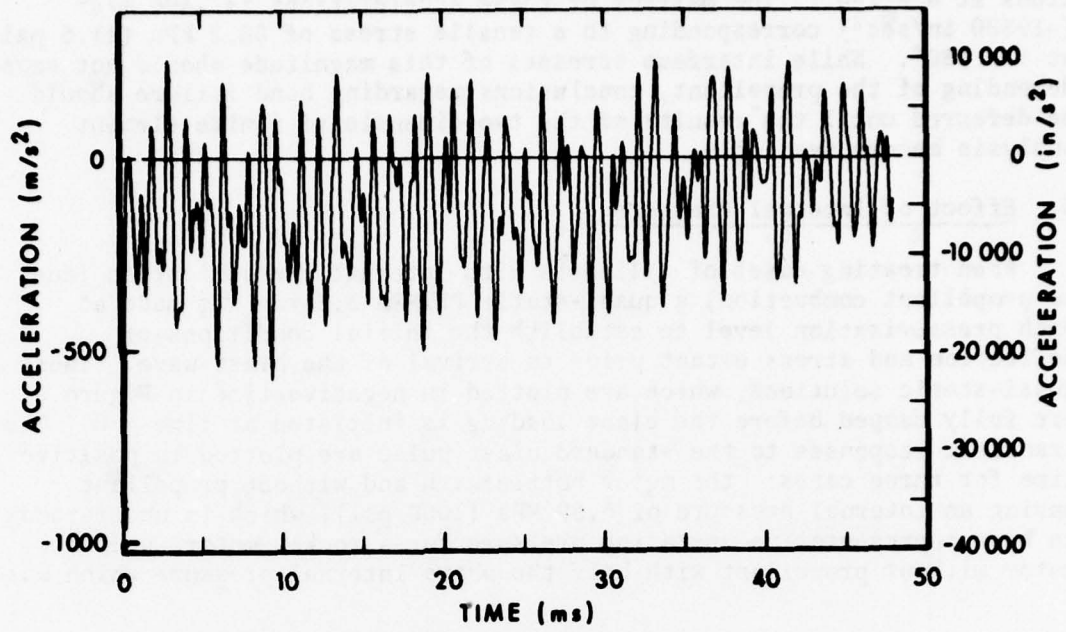

Figure 7. Acceleration at θ = 0° for Unpressurized Motor Case Containing Propellant

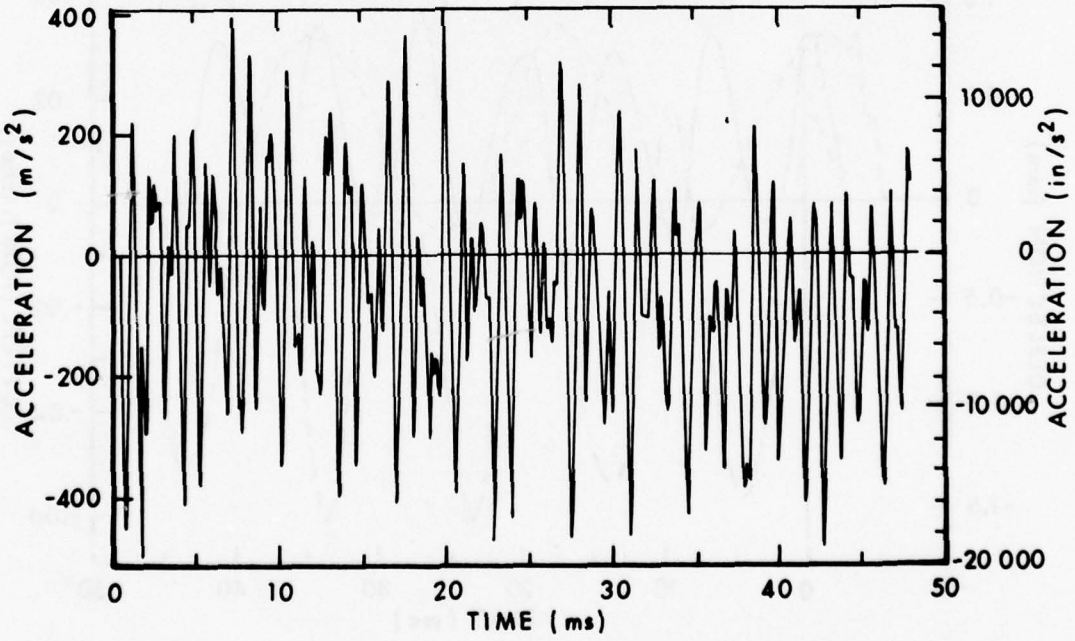

Figure 8. Acceleration at θ = 180° for Unpressurized Motor Case Containing Propellant

associated with positive accelerations at $\theta = 0°$ and negative accelerations at $\theta = 180°$. The maximum of these accelerations is -496 m/s^2 (-19500 in/sec^2) corresponding to a tensile stress of 80.2 kPa (11.6 psi) at $\theta = 180°$. While interface stresses of this magnitude should not cause debonding of the propellant, conclusions regarding bond failure should be deferred until the results of the two-dimensional finite element analysis become available.

B. Effect of Internal Pressure

When treating cases of cylinders with internal pressurization (due to propellant combustion) a quasi-static PETROS 3.5 run was made at each pressurization level to establish the initial conditions of deflection and stress extant prior to arrival of the blast wave. These quasi-static solutions, which are plotted in negative time in Figure 9, are fully damped before the blast loading is initiated at time = 0. The transient responses to the standard blast pulse are plotted in positive time for three cases: the motor bottle with and without propellant having an internal pressure of 6.89 MPa (1000 psi), which is understood to be a representative operating pressure for a rocket motor, and the motor without propellant with half the above internal pressure which was

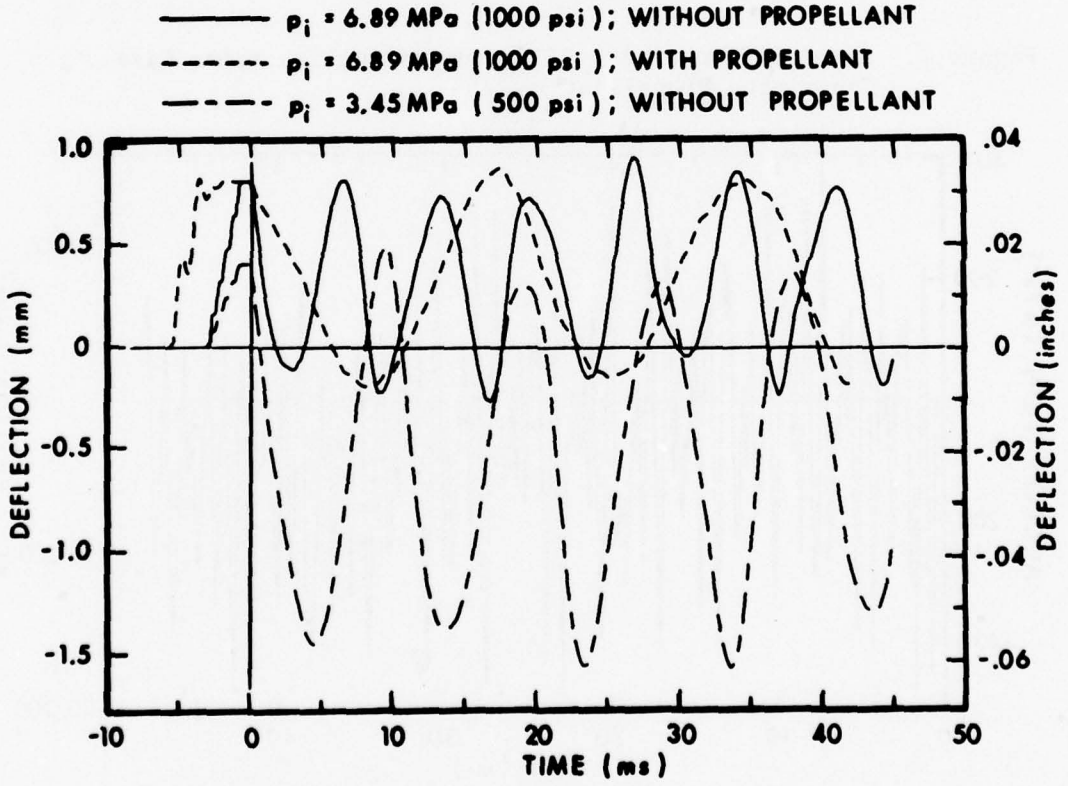

Figure 9. Deflection at $\theta = 0°$ with Internal Pressurization

run to study the effect of varying the internal pressure. One sees that increasing the internal pressure raises the frequency of oscillation and decreases the amplitude of response (provided the shell remains elastic). At the operating pressure adding propellant lowers the frequency of response and has little effect on the amplitude.

Figure 10 presents cross section views of cylinder response at two times for the case represented by the solid curve in Figure 9. In these views the departure from the initial unpressurized configuration has been magnified by a factor of one hundred. For Cycle 0 we see the axisymmetric extensional deformation pattern which exists immediately before the arrival of the blast loading. With the 6.89 MPa (1000 psi) internal pressure the circumferential membrane stress is 91 percent of the uniaxial yield stress while the maximum bending stresses are less than one percent of this quantity. The cross section for Cycle 377, which may be associated with the second inward peak displacement shown in Figure 9, exhibits an essentially inextensional flexural deformation superposed upon the extensional pattern for Cycle 0. The corresponding quasi-static and transient strains at the crown line are depicted in Figure 11. Clearly, the blast-induced strain fluctuations are small in comparison to the pressurization-induced strain. In fact, in spite of the large pre-stressing, none of the problems treated in Figure 9 were predicted to experience permanent deformation of the motor case as a result of the blast loading.

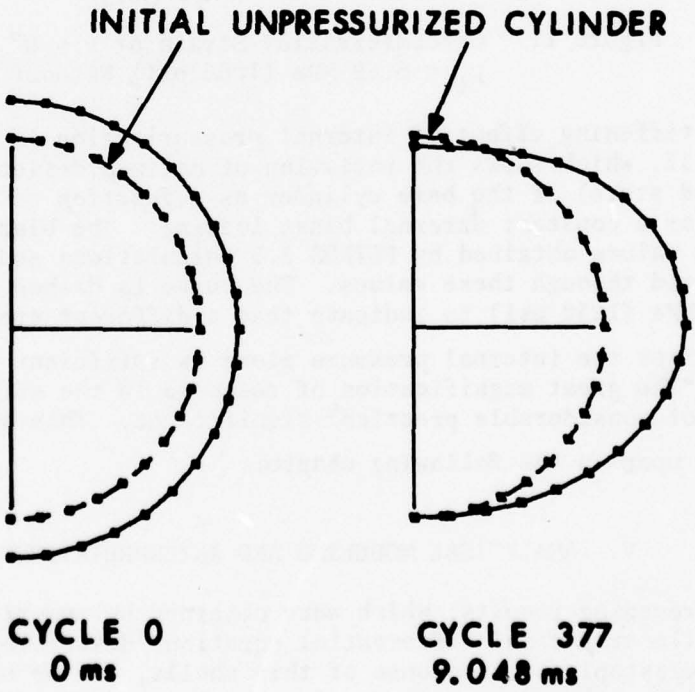

Figure 10. Cross Sections of Pressurized Cylinder

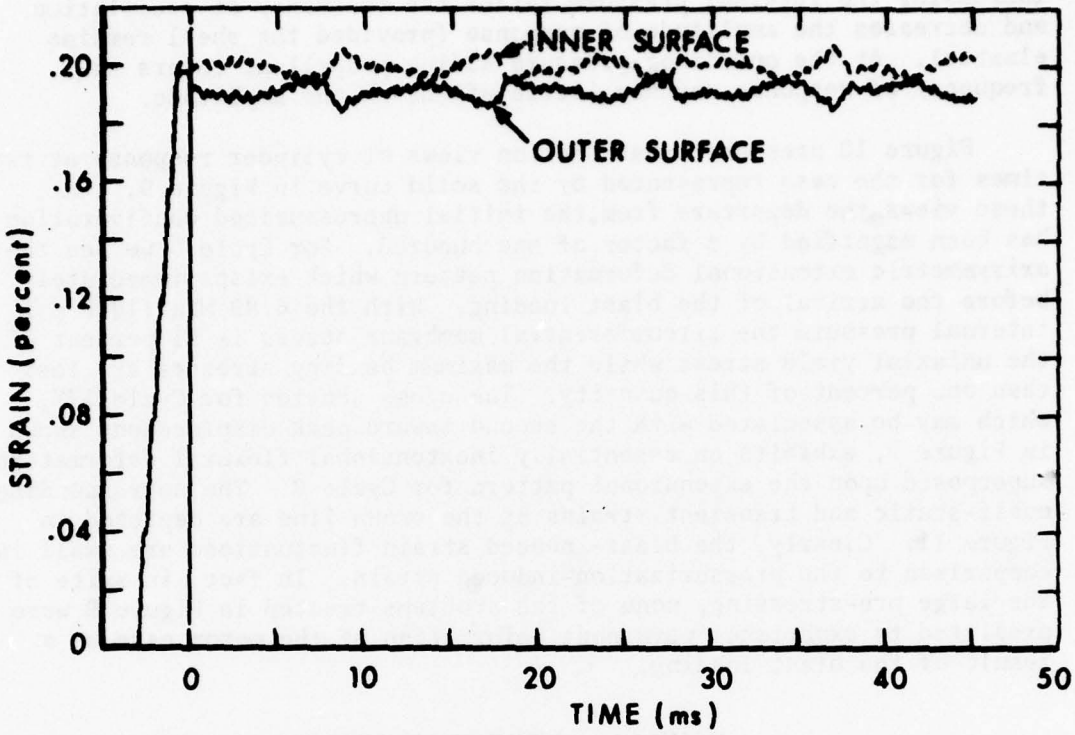

Figure 11. Circumferential Strain at $\theta = 0°$ for p_i = 6.89 MPa (1000 psi) Without Propellant

The stiffening effect of internal pressurization is demonstrated in Figure 12, which shows the variation of maximum deflection (from the pressurized state) of the bare cylinder as a function of internal pressure for a constant external blast loading. The black dots on this figure are values obtained by PETROS 3.5 calculations and the curve is a line faired through these values. The curve is dashed beyond p_i = 8.48 MPa (1230 psi) to indicate that a different trend may be expected after the internal pressure alone is sufficient to produce yielding. The great magnification of response in the neighborhood of $p_i = 0$ is of considerable practical significance. This subject will be elaborated upon in the following chapter.

V. ANALYTICAL MODELING AND INTERPRETATIONS

The preceding results, which were obtained by numerical solution of the nonlinear partial differential equations describing finite amplitude elastoplastic response of thin shells, can be usefully interpreted by comparison with the deductions from an exact analysis of a linearized formulation for the same problem. Although several

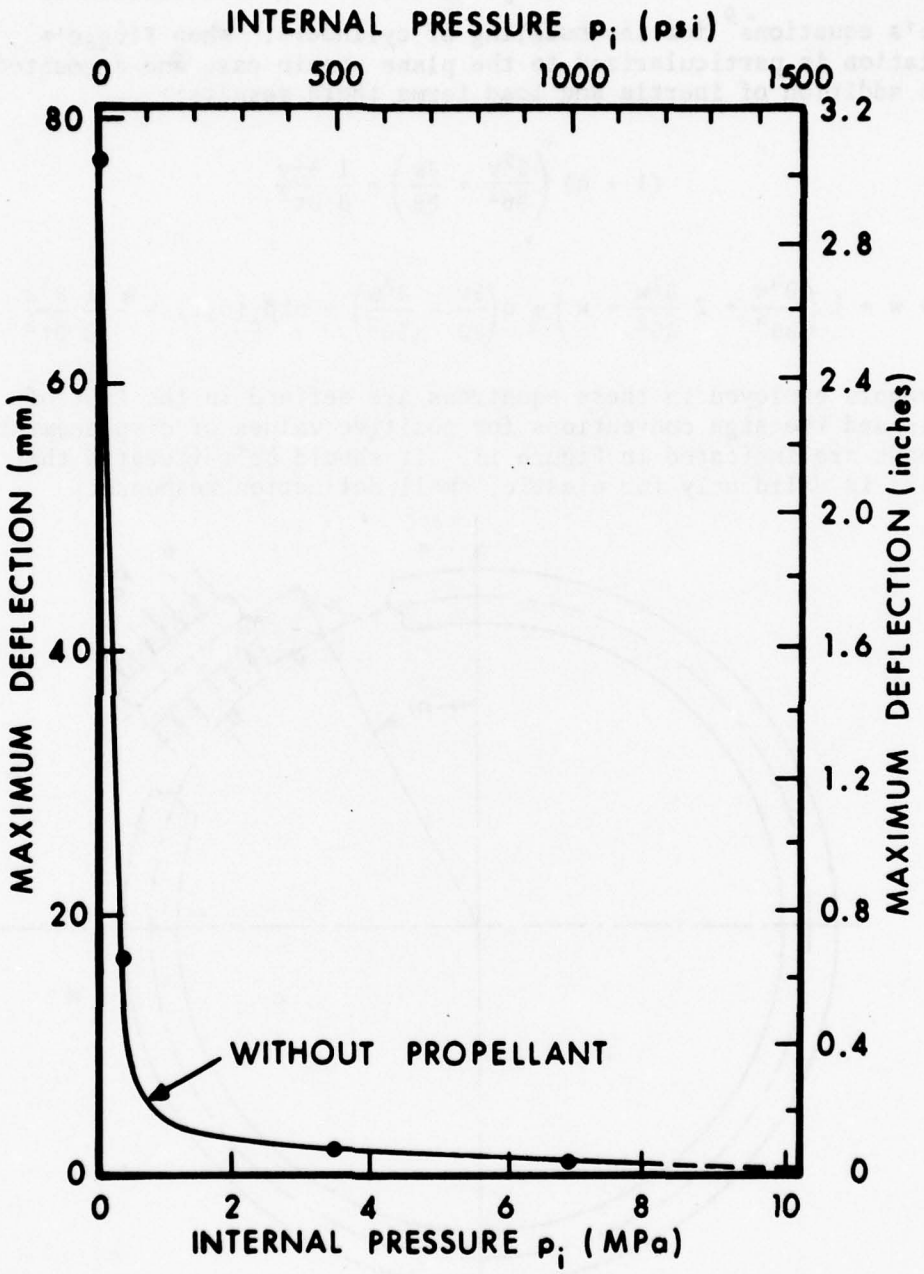

Figure 12. Effect of Internal Pressure on Peak Response

alternate versions of the latter formulation were investigated it appears that the simplest theoretical development which contains all the desired features can best be presented as a generalization of Flügge's equations[9] for the buckling of cylinders. When Flügge's formulation is particularized to the plane strain case and augmented by the addition of inertia and load terms there results:

$$(1 + q)\left(\frac{\partial^2 v}{\partial \theta^2} + \frac{\partial w}{\partial \theta}\right) = \frac{1}{\beta}\frac{\partial^2 v}{\partial t^2} \tag{5}$$

$$\frac{\partial v}{\partial \theta} + w + k\left(\frac{\partial^4 w}{\partial \theta^4} + 2\frac{\partial^2 w}{\partial \theta^2} + w\right) + q\left(\frac{\partial v}{\partial \theta} - \frac{\partial^2 w}{\partial \theta^2}\right) + \alpha k p_e(\theta,t) = -\frac{1}{\beta}\frac{\partial^2 w}{\partial t^2} \tag{6}$$

The symbols employed in these equations are defined in the List of Symbols and the sign conventions for positive values of displacements and loads are indicated in Figure 13. It should be reiterated that this analysis is valid only for elastic, small deflection response.

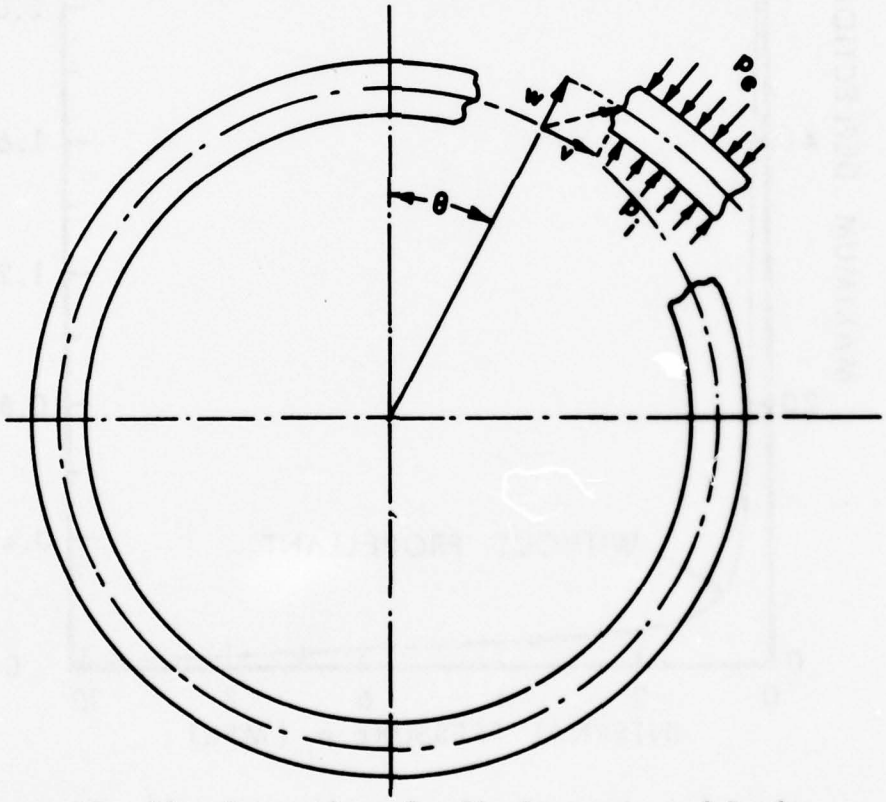

Figure 13. Sign Conventions for Displacements and Loads

[9] *W. Flügge, "Stresses in Shells", Second Edition, Springer-Verlag, 1973, p. 448.*

If desired, one can eliminate the tangential displacement v and obtain a single differential equation for the radial displacement w. To accomplish this, Equation (5) is differentiated with respect to θ and Equation (6) is solved for $\frac{\partial v}{\partial \theta}$:

$$(1 + q)\left(\frac{\partial^3 v}{\partial \theta^3} + \frac{\partial^2 w}{\partial \theta^2}\right) = \frac{1}{\beta}\frac{\partial^3 v}{\partial \theta \partial t^2} \tag{7}$$

$$\frac{\partial v}{\partial \theta} = \frac{1}{1 + q}\left[- w - k\left(\frac{\partial^4 w}{\partial \theta^4} + 2\frac{\partial^2 w}{\partial \theta^2} + w\right) + q\frac{\partial^2 w}{\partial \theta^2} - \alpha k p_e - \frac{1}{\beta}\frac{\partial^2 w}{\partial t^2}\right] \tag{8}$$

Successive differentiation of Equation (8) yields the terms needed for substitution in Equation (7); when this is accomplished and terms are collected one obtains:

$$\frac{\partial^6 w}{\partial \theta^6} + \left(2 - \frac{q}{k}\right)\frac{\partial^4 w}{\partial \theta^4} + \left(1 - \frac{q}{k}\right)\frac{\partial^2 w}{\partial \theta^2} + \alpha\frac{\partial^2 p_e}{\partial \theta^2}$$

$$= \frac{1}{\beta(1+q)}\left[\frac{\partial^6 w}{\partial \theta^4 \partial t^2} + \left\{2\left(1 - \frac{q}{k}\right) - \frac{1}{k}\right\}\frac{\partial^4 w}{\partial \theta^2 \partial t^2} + \left(\frac{1+k}{k}\right)\frac{\partial^2 w}{\partial t^2} + \frac{1}{\beta k}\frac{\partial^4 w}{\partial t^4} + \alpha\frac{\partial^2 p_e}{\partial t^2}\right] \tag{9}$$

A. Free Vibrations

Before attempting a solution of Equation (9) for the forced response of the cylinder it is expedient to consider the free vibration characteristics of the system defined by the preceding equations. Setting $p_e = 0$ in Equation (9) and substituting

$$w = \sum_n w_n \cos n\theta \sin \omega_n t \tag{10}$$

demonstrates that the function cos $n\theta$ is an eigenfunction* and leads to the frequency equation:

$$\omega_n = \left[\frac{\beta}{2}\left\{1 + (1+2q)n^2 + k(1-n^2)^2 \pm \left[(1+n^2)^2 + 4(2+q)qn^2 + 2k(1-n^2)^3 + k^2(1-n^2)^4\right]^{\frac{1}{2}}\right\}\right]^{\frac{1}{2}} \tag{11}$$

n takes on integral values. Sin $n\theta$ is also an eigenfunction but, since we are concerned only with modes symmetric with respect to $\theta=0$, no use will be made of this function.

Equation (11) reveals that there are two natural frequencies associated with each value of n. Consequently in the sequel the frequencies will carry two subscripts; e.g., $\omega_{n,s}$, where s = 1 or 2. Further, it should not be assumed that the v and w components of displacement are independent. If the radial component of the n^{th} mode is assumed to be

$$w_n = \cos n\theta \, (w_{n,1} \sin \omega_{n,1} t + w_{n,2} \sin \omega_{n,2} t) \tag{12}$$

where $w_{n,1}$ and $w_{n,2}$ are arbitrary amplitude coefficients, then the tangential displacements in the same mode must have the form

$$\begin{aligned} v_n = \frac{\sin n\theta}{2(1+q)n} \Bigg\{ & \Big[(n^2-1)\{1-k(n^2-1)\} \\ & - \Big\{ (n^2+1)^2 + 4(2+q)qn^2 - 2k(n^2-1)^3 + k^2(n^2-1)^4 \Big\}^{\frac{1}{2}} \Big] w_{n,1} \sin \omega_{n,1} t \\ & + \Big[(n^2-1)\{1-k(n^2-1)\} \\ & + \Big\{ (n^2+1)^2 + 4(2+q)qn^2 - 2k(n^2-1)^3 + k^2(n^2-1)^4 \Big\}^{\frac{1}{2}} \Big] w_{n,2} \sin \omega_{n,2} t \Bigg\} \end{aligned} \tag{13}$$

in order that v_n, w_n satisfy Equations (7) and (8) simultaneously. Since either of the amplitude coefficients $w_{n,1}$ or $w_{n,2}$ can be taken to be zero, it is clear that there are two distinct families of modes having frequencies $\omega_{n,1}$ and $\omega_{n,2}$, the lower frequency family being identified with s = 1.

Certain useful characterizations of these two families of vibration modes can be achieved by substitution of their individual displacement components into the expressions for circumferential membrane strain

$$\bar{\varepsilon}_\theta = \frac{1}{a}\left(\frac{\partial v}{\partial \theta} + w\right) \tag{14}$$

and for circumferential bending moment

$$M_\theta = \frac{Eh^3}{12(1-\nu^2)a^2}\left(\frac{\partial^2 w}{\partial \theta^2} + w\right) \tag{15}$$

For the s = 1 modes with $n \geq 2$ the membrane strains are insignificantly small while the bending moments are appreciable. Thus, this lower frequency set of modes can be identified as the family of inextensional bending modes of a cylinder. The special cases for n = 0 and n = 1 (for s = 1) are not vibratory modes; n = 0 corresponds to a static expansion or contraction of the cylinder while n = 1 represents a rigid body translation of the cylinder cross section along the $\theta = 0$ axis.

The s = 1 family of modes is extremely sensitive to the internal pressure p_i as illustrated in Figure 14 for the lower natural frequencies $f_{n,1} (= \omega_{n,1}/2\pi)$. The frequency of the fundamental inextensional mode $f_{2,1}$ is seen to have an intercept on the p_i axis at -0.214 MPa (-31.1 psi) corresponding to the value of uniformly distributed external pressure for which static buckling* of the cylinder would occur in the cos 2θ mode. The great magnification of response in the neighborhood of $p_i = 0$ exhibited in Figure 12 can be explained on this

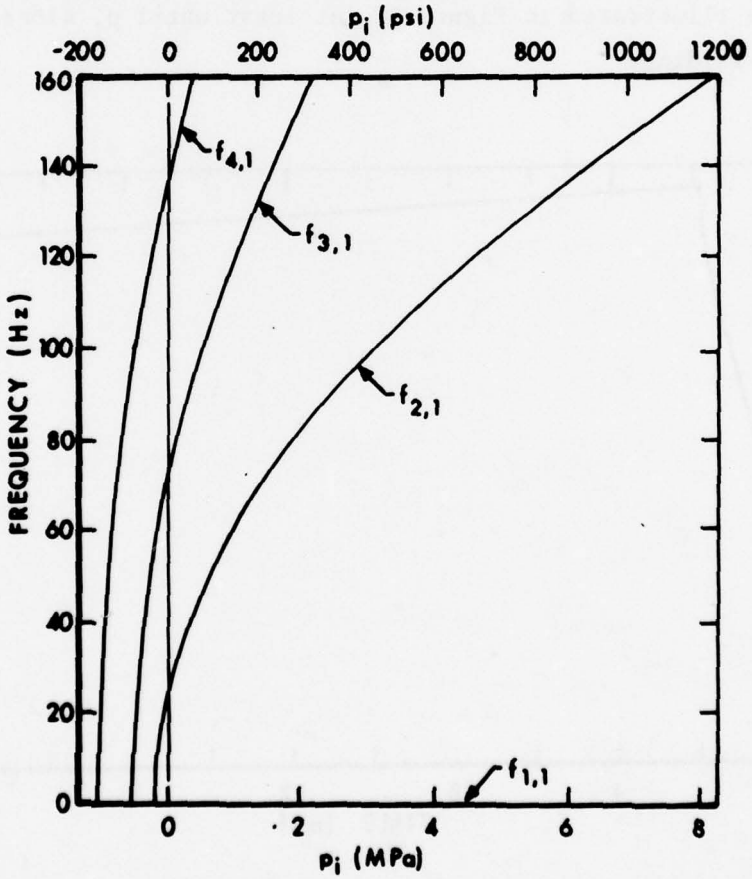

Figure 14. Effect of Internal Pressure on Certain Inextensional Mode Frequencies

*See Reference 9, pp. 459-60.

basis. The actual blast loading can be decomposed into a transient uniformly distributed external pressure and a non-uniform transient loading. The latter serves to deform the cylinder from the initial circular cross section (analogous to a large initial imperfection) while the uniform component provides a nonlinear amplification of response if its magnitude is a significant fraction of the pressure required for static buckling. For the blast loading employed in the PETROS 3.5 calculations the temporal variation of the uniform component is shown in Figure 15. This pressure component reaches a maximum of 0.119 MPa (17.3 psi), which is 56% of the static buckling pressure, and decays slowly with respect to the period of the fundamental bending mode (39.3 ms) so there is ample time for a large deflection to occur. The response for $p_i = 0$ was also enhanced by the increased flexibility associated with plastic flow. For large internal pressurization the circumferential membrane stresses remain tensile in spite of the blast loading so there is no near-buckling effect. In fact, consonant with the raising of the frequency spectrum of the inextensional modes with increasing p_i, as shown in Figure 14, there is the decrease in response amplitude illustrated in Figure 12 (at least until p_i alone causes plastic yielding).

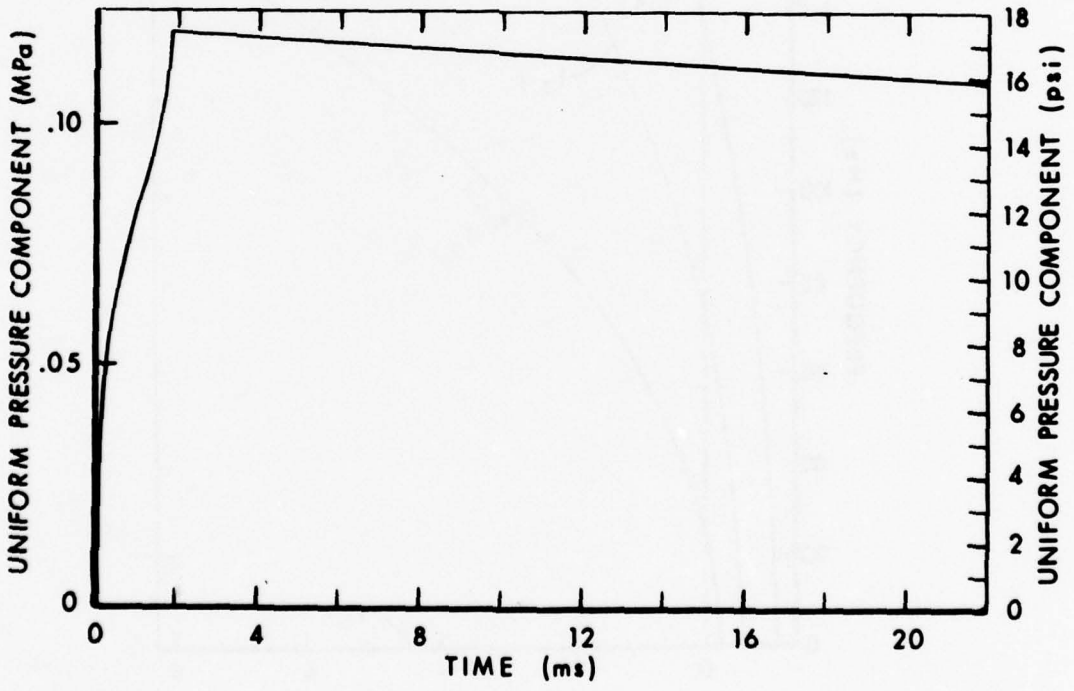

Figure 15. Variation of Mean External Pressure

An interesting correlation between analytical and numerical predictions is shown in Figure 16. The circled points represent periods $\tau_{2,1}$ ($= 2\pi/\omega_{2,1}$) of post-peak elastic oscillations measured from plots of PETROS 3.5 calculations for various values of p_i. The solid curve is the analytical prediction of variation of period with internal pressure obtained with the aid of Equation (11). The agreement is amazingly good for the two larger values of p_i and the deviations at the two lower internal pressurizations can be readily explained. At these lower values of p_i the mean value of the external blast loading depicted in Figure 16 is large enough relative to p_i to produce a small negative shift in the effective value of the abscissas for the circled points (which would produce better agreement with the solid curve).

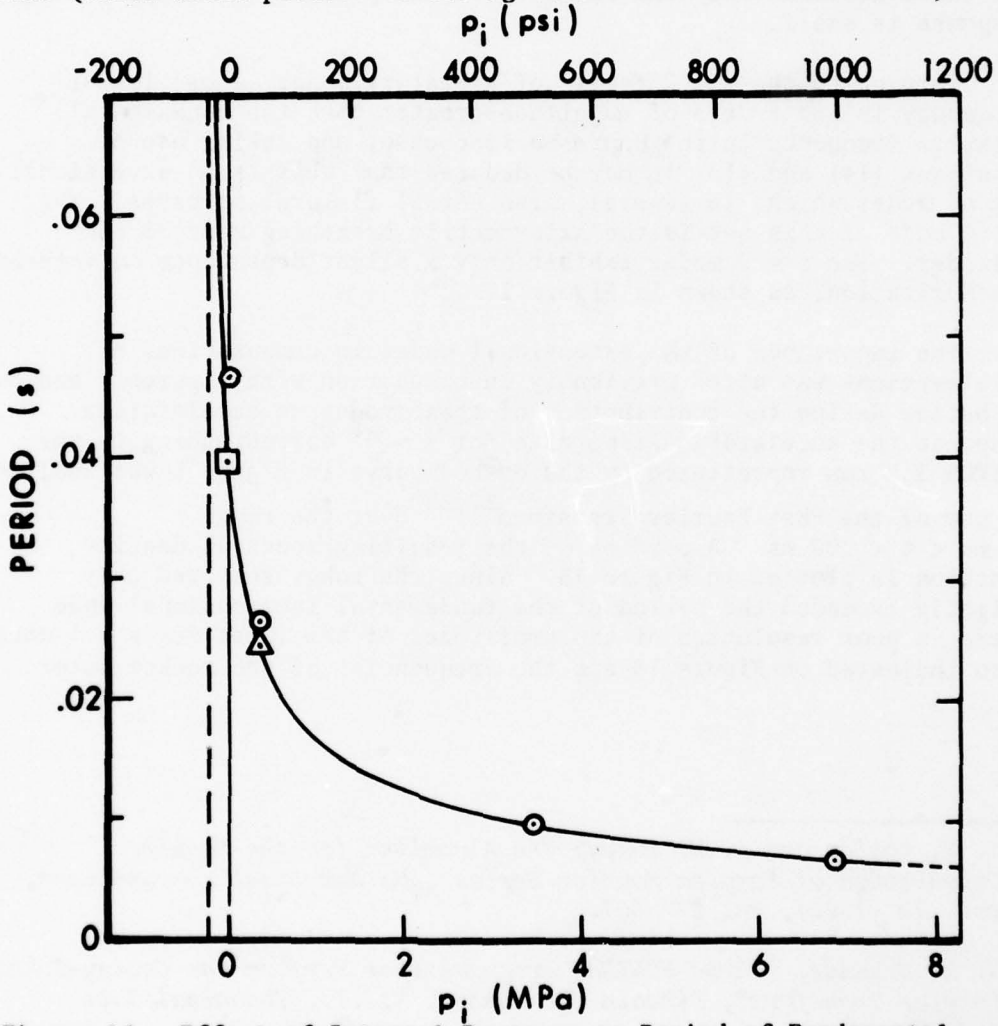

Figure 16. Effect of Internal Pressure on Period of Fundamental Inextensional Mode

To verify this deduction the following tests were performed. At p_i = 0.345 MPa (50 psi) the PETROS 3.5 code was run to obtain static equilibrium, then instead of applying the blast loading, the numerical solution was restarted with an initial velocity distribution corresponding to the (2,1) mode with an amplitude such as to produce a response approximately equal to that produced by the blast loading. The post-peak vibratory period was found to be that surrounded by the small triangle. At p_i = 0 a PETROS 3.5 run was made with the blast loading scaled down to a peak value of 6.89 kPa (1 psi) so that the mean component of the blast loading was negligible and the response amplitude was small. This led to the free vibration period enclosed by the small square. Thus it has been demonstrated that there is essentially perfect agreement between the analytically predicted eigenfrequencies and those determined by the PETROS 3.5 code provided the amplitude of response is small.

Turning to the s = 2 family of vibratory modes, whose lowest frequency is two orders of magnitude greater than the fundamental flexural frequency in the unpressurized case, and making use of Equations (14) and (15) it may be deduced that this is an extensional set of modes which, in general, also entail flexural stresses. The n = 0 mode of this set is the axisymmetric breathing mode of the cylinder. The s = 2 modes exhibit only a slight dependence on internal pressurization, as shown in Figure 17.

The importance of the extensional modes in computations of accelerations was cited previously in connection with Figures 7 and 8. To better define the contribution of these modes to acceleration response the acceleration-time data for $\theta = 0°$ corresponding to the PETROS 3.5 run represented by the dashed curve in Figure 5 was analyzed by use of the Fast Fourier Transform[10,11] over the range 80 ms < t < 200 ms. A portion of the resulting spectral density function is plotted in Figure 18. Since the range selected only slightly exceeded the period of the fundamental inextensional mode there is poor resolution of the amplitudes of the first few s = 1 modes. Also indicated on Figure 18 are the frequencies of the rocket motor

---

[10] *J. W. Cooley and J. W. Tukey, "An Algorithm for the Machine Calculation of Complex Fourier Series", Mathematical Computations, vol. 19 (1965), pp. 297-301.*

[11] *N. M. Brenner, "Three FORTRAN Programs that Perform the Cooley-Tukey Fourier Transform", Lincoln Laboratory, M.I.T., Technical Note 1967-2.*

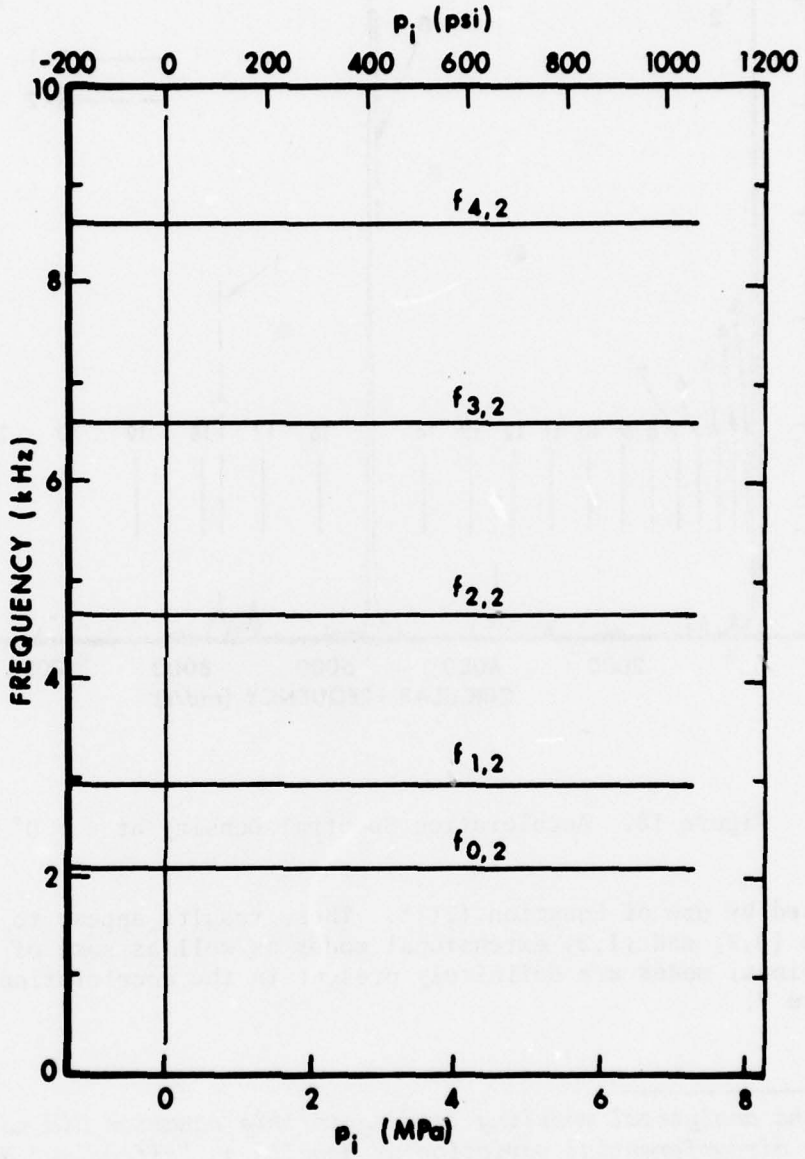

Figure 17. Effect of Internal Pressure on Frequencies of Extensional Modes

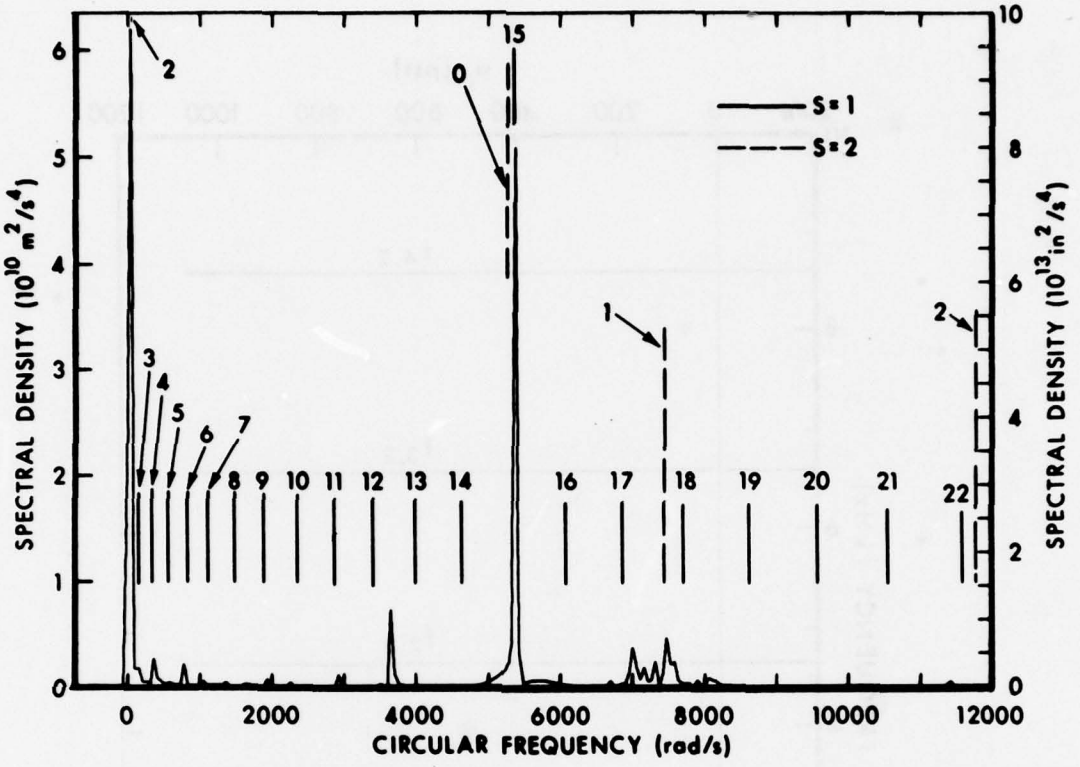

Figure 18. Acceleration Spectral Density at $\theta = 0°$

calculated by use of Equation (11)*. These results appear to confirm that the (0,2) and (1,2) extensional modes as well as some of the inextensional modes are definitely present in the acceleration response of Figure 7.

Since the analytical modeling leading to this equation did not provide for any circumferential variation of density an "effective" uniform density was employed based on the total mass of motor case plus propellant. This approximation, which "smears out" the inhomogeneity associated with the slots in the propellant, is not believed to introduce any large error in the frequency predictions for small values of n.

B. Forced Vibrations

The response of the plane strain cylinder to the prescribed blast loading has been analyzed in the classical manner, representing both the applied loading and the radial deflections by infinite series in the free vibration eigenfunctions:

$$p_e(\theta,t) = \sum_{n=0}^{\infty} p_n(t) \cos n\theta \tag{16}$$

$$w(\theta,t) = \sum_{n=0}^{\infty} w_n(t) \cos n\theta \tag{17}$$

The coefficients for the load series may be determined from

$$p_0(t) = \frac{1}{\pi} \int_0^{\pi} p_e(\theta,t)\, d\theta \tag{18}$$

$$p_n(t) = \frac{2}{\pi} \int_0^{\pi} p_e(\theta,t) \cos n\theta\, d\theta \quad \text{for } n \geq 1 \tag{19}$$

When the specific load function of Equation (1) is introduced into Equations (18) and (19) and the integrals are evaluated (numerically) the values of $p_n(t)$ shown in Figure 19 are obtained. The intent in presenting this Figure is not to present quantitative values of the coefficients but merely to show that their variation is reasonable and that their amplitudes decrease monotonically after full envelopment of the cylinder by the blast wave, indicating a reasonable rate of convergence for the series of Equation (16).

As a check upon the adequacy of the Fourier representation of the applied loading given by Equation (16), plots were made comparing the initial blast loading of Equation (1) with 10- and 20- term Fourier representations at various times during and after the diffraction phase of loading. Three of these plots are shown in Figure 20. It may be seen that at the early stages of envelopment the maximum number of terms in the series representation is desirable whereas, at later times, fewer terms would be adequate. However, for results to be presented subsequently, the full 20 - term series was employed.

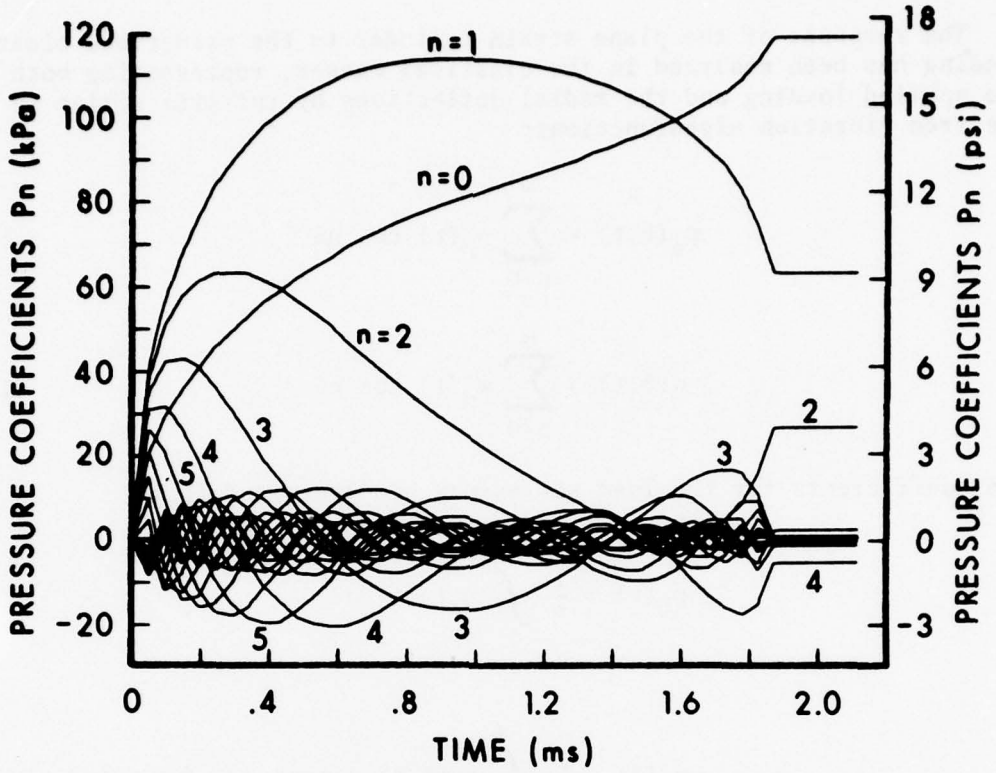

Figure 19. Transient Values of External Load Coefficients

When the expressions for p_e and w given by Equations (16) and (17) are substituted into Equation (9) to effect a separation of variables the following ordinary differential equations for the coefficients $w_n(t)$ are obtained:

$$\ddot{\ddot{w}}_n + \beta k\left[n^4 - \left\{2\left(1 - \frac{q}{k}\right) - \frac{1}{k}\right\}n^2 + \frac{1+k}{k}\right]\ddot{w}_n$$

$$+ \beta^2 k(1+q)n^2\left\{n^4 - \left(2 - \frac{q}{k}\right)n^2 + 1 - \frac{q}{k}\right\} w_n = -\alpha\beta k\left\{\ddot{p}_n + \beta(1+q)n^2 p_n\right\} \quad (20)^*$$

$$n = 0,1,2,3,.....$$

*A dot over a variable indicates differentiation with respect to time.

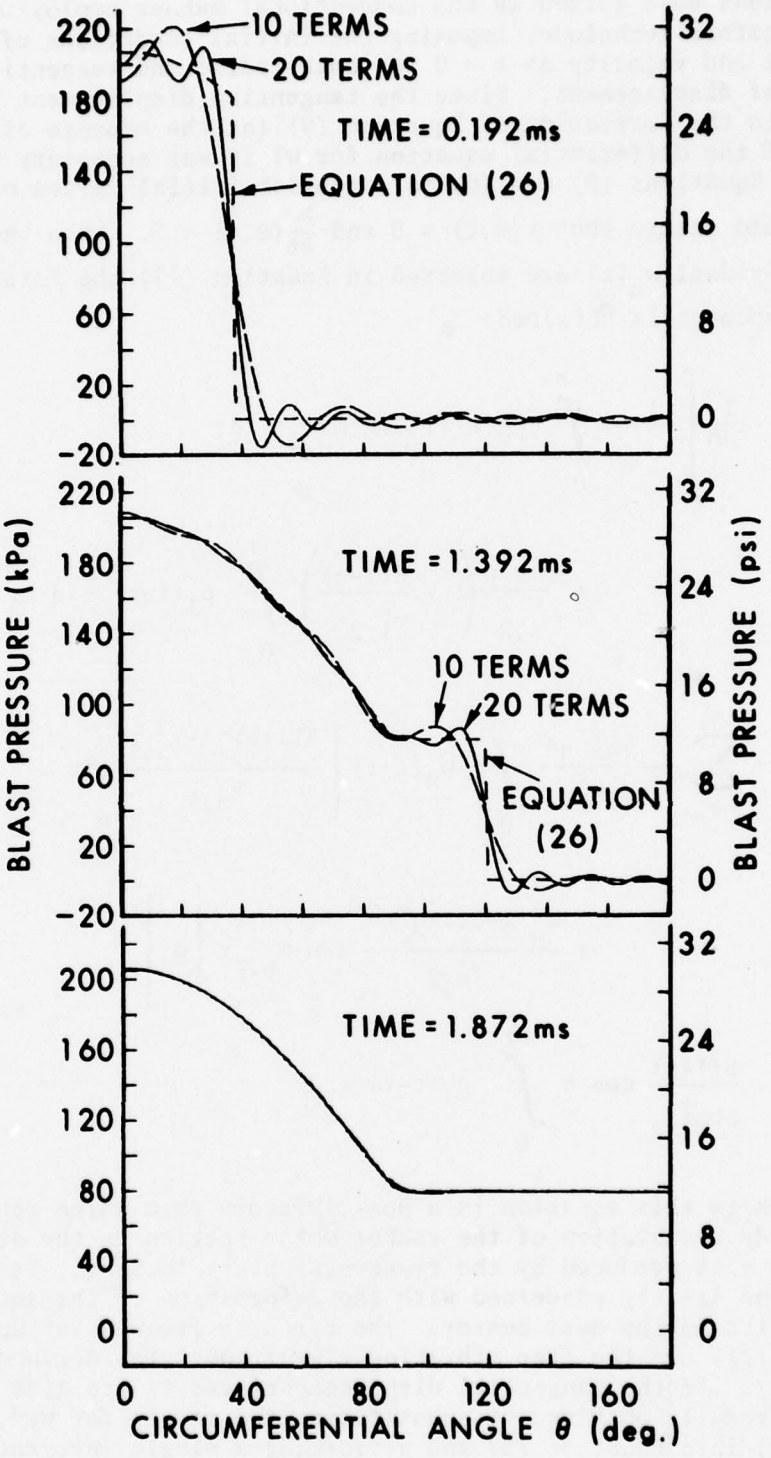

Figure 20. Fourier Representations of Pressure Distributions

These equations were solved in the conventional manner employing the Laplace transform technique, imposing the initial conditions of zero displacement and velocity at t = 0 for both radial and tangential components of displacement. Since the tangential displacement v was eliminated in the derivation of Equation (9) (at the expense of raising the order of the differential equation for w) it was necessary to have recourse to Equations (5) and (6) to establish initial values of $\ddot{w}_n$ and $\dddot{w}_n$ which would ensure that $v(\theta,t) = 0$ and $\frac{\partial v}{\partial t}(\theta,t) = 0$. When the solutions for the individual $w_n(t)$ are inserted in Equation (17) the total radial response component is obtained:

$$w(\theta,t) = -\frac{1}{\rho h}\left[\frac{1}{\omega_{0,2}}\int_0^t p_0(t-\tau)\sin\omega_{0,2}\tau\,d\tau\right.$$

$$+\frac{\cos\theta}{\omega_{1,2}}\left(1-\frac{\beta(1+q)}{\omega_{1,2}^2}\right)\int_0^t p_1(t-\tau)\sin\omega_{1,2}\tau\,d\tau$$

$$+\sum_{n=2}^{\infty}\frac{\cos n\theta}{\omega_{n,2}^2-\omega_{n,1}^2}\int_0^t p_n(t-\tau)\left\{\frac{\beta(1+q)n^2-\omega_{n,1}^2}{\omega_{n,1}}\sin\omega_{n,1}\tau\right. \qquad (21)$$

$$\left.\left.+\frac{\omega_{n,2}^2-\beta(1+q)n^2}{\omega_{n,2}}\sin\omega_{n,2}\tau\right\}d\tau\right]$$

$$-\frac{\beta(1+q)}{\rho h\omega_{1,2}^2}\cos\theta\int_0^t p_1(t-\tau)\,\tau\,d\tau$$

The last term in this equation is a non-vibratory term which represents the rigid body translation of the rocket motor section in the direction of the $\theta = 0$ axis produced by the transverse blast loading. It may be omitted if one is only concerned with the deformation of the section relative to its moving mass center. The circular frequencies appearing in Equation (21) are the free vibration eigenfrequencies defined by Equation (11). If the tangential displacements $v(\theta,t)$ are also desired they may be readily obtained by substituting the result for $w(\theta,t)$ from Equation (21) into Equation (8) and performing a single integration with respect to θ.

A digital computer program has been written to facilitate the use of Equation (21). This program evaluates the convolution integrals appearing therein by numerical integration for prescribed pressure coefficients $p_n(t)$, such as those displayed in Figure 19. This formulation is quite satisfactory provided $w(\theta,t)$ is to be evaluated for only a few values of time. However, if w is to be calculated for numerous values of t (e.g., to obtain data for a time-wise plot of w) the evaluation of the convolution integrals over the range $0 \leq \tau \leq t$ becomes costly and wasteful. This difficulty can be circumvented by use of the following computational algorithm. Equation (21) contains numerous integrals of the type

$$\int_0^t p_n(t-\tau) \sin \omega_{n,s}\tau \, d\tau = \int_0^t p_n(\tau) \sin \omega_{n,s}(t-\tau) \, d\tau$$

$$= \sin \omega_{n,s}t \int_0^t p_n(\tau) \cos \omega_{n,s}\tau \, d\tau \qquad (22)$$

$$- \cos \omega_{n,s}t \int_0^t p_n(\tau) \sin \omega_{n,s}\tau \, d\tau$$

Let the time interval $0 \leq \tau \leq t$ be divided into increments Δt such that $m\Delta t = t$ and introduce the notation

$$\Delta C^j_{n,s} = \int_{(j-1)\Delta t}^{j\Delta t} p_n(\tau) \cos \omega_{n,s}\tau \, d\tau \qquad (23)$$

$$\Delta S^j_{n,s} = \int_{(j-1)\Delta t}^{j\Delta t} p_n(\tau) \sin \omega_{n,s}\tau \, d\tau \qquad (24)$$

$$C_{n,s}(t) = \int_0^{m\Delta t} p_n(\tau) \cos \omega_{n,s}\tau \, d\tau = C^m_{n,s} \qquad (25)$$

$$S_{n,s}(t) = \int_0^{m\Delta t} p_n(\tau) \sin \omega_{n,s}\tau \, d\tau = S^m_{n,s} \tag{26}$$

Equation (25) may be written

$$\begin{aligned} C^m_{n,s} &= \int_0^{(m-1)\Delta t} p_n(\tau) \cos \omega_{n,s}\tau \, d\tau + \int_{(m-1)\Delta t}^{m\Delta t} p_n(\tau) \cos \omega_{n,s}\tau \, d\tau \\ &= C^{m-1}_{n,s} + \Delta C^m_{n,s} \\ &= \sum_{j=1}^{m-1} \Delta C^j_{n,s} + \Delta C^m_{n,s} = \sum_{j=1}^{m} \Delta C^j_{n,s} \end{aligned} \tag{27}$$

Thus $C_{n,s}(t)$ can be evaluated by accumulating the sum of the $\Delta C^j_{n,s}$ to obtain $C^{m-1}_{n,s}$ and then only having to calculate $\Delta C^m_{n,s}$ (by numerical integration unless the interval Δt is taken so small that a cruder approximation suffices) for the current Δt. The same procedure can be applied for calculation of $S_{n,s}(t)$. Then Equation (21) can be rewritten as:

$$\begin{aligned} w(\theta,t) = -\frac{1}{\rho h} \Bigg[& \frac{1}{\omega_{0,2}} \left(C^m_{0,2} \sin \omega_{0,2}t - S^m_{0,2} \cos \omega_{0,2}t \right) \\ & + \left(1 - \frac{\beta(1+q)}{\omega^2_{1,2}} \right) \frac{\cos\theta}{\omega_{1,2}} \left(C^m_{1,2} \sin \omega_{1,2}t - S^m_{1,2} \cos \omega_{1,2}t \right) \\ & + \sum_{n=2}^{\infty} \frac{\cos n\theta}{\omega^2_{n,2} - \omega^2_{n,1}} \Bigg\{ \frac{\beta(1+q)n^2 - \omega^2_{n,1}}{\omega_{n,1}} \left(C^m_{n,1} \sin \omega_{n,1}t - S^m_{n,1} \cos \omega_{n,1}t \right) \\ & + \frac{\omega^2_{n,2} - \beta(1+q)n^2}{\omega_{n,2}} \left(C^m_{n,2} \sin \omega_{n,2}t - S^m_{n,2} \cos \omega_{n,2}t \right) \Bigg\} \Bigg] \\ & - \frac{\beta(1+q)}{\rho h \omega^2_{1,2}} \cos\theta \int_0^t (t-\tau) \, p_1(\tau) \, d\tau \end{aligned} \tag{28}$$

The computer program which was developed for evaluation of Equation (21) has been modified to incorporate this algorithm.

C. Transient Response Correlations

A comparison of deflections at $\theta = 0$ obtained with the PETROS 3.5 code and with Equation (28) of the analytical solution is shown in Figure 21 for the standard blast load applied to the bare motor case with p_i = 6.89 MPa (1000 psi). The blast wave arrives at the pre-pressurized shell at t = 0, driving the shell at $\theta = 0$ inwards and exciting the vibratory response which follows. The agreement between these two solutions is entirely satisfactory for engineering purposes in this case of small amplitude response where the linear elastic analysis should be valid. In fact, the analytical solution should give accurate results for all values of p_i to the right of the "knee" of the curve in Figure 12. Conversely, one would not expect it to provide accurate results where the amplitude of response is large and this is borne out by the comparison of responses for $p_i = 0$ shown in Figure 22*.

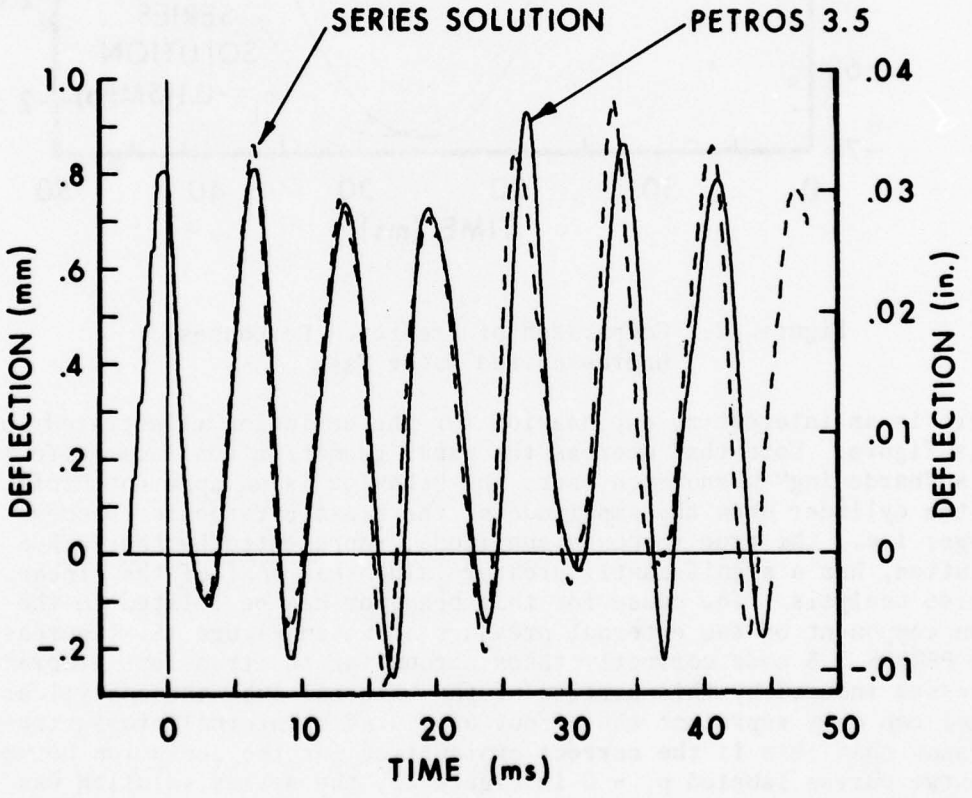

Figure 21. Comparison of Predicted Responses for Pressurized Motor Case

For this comparison (unlike the result shown in Figure 5) the yield stress of the motor case material was made very large so that the PETROS 3.5 solution remained elastic, thus providing a proper basis for comparison with the series solution.

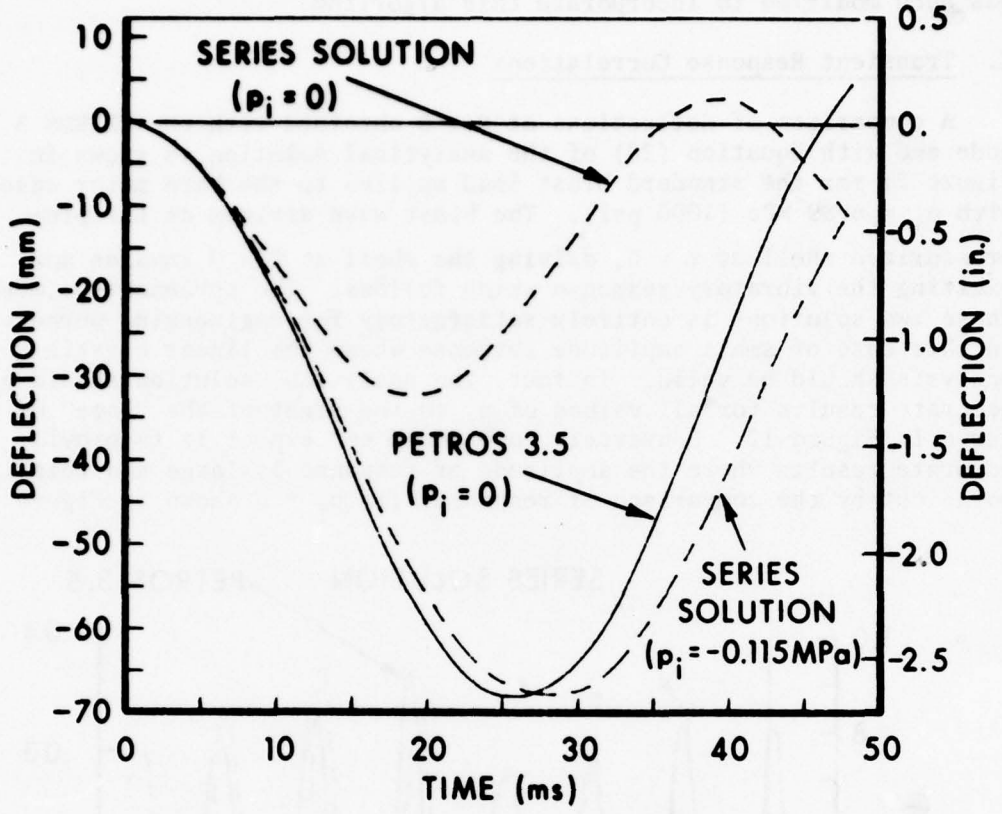

Figure 22. Comparison of Predicted Responses of Unpressurized Motor Case

There is an interesting explanation for the deviation illustrated in this figure. Note that whereas the usual geometric nonlinear effect is a "hardening" phenomenon, here the behavior is an apparent "softening" of the cylinder when the amplitude of the elastic response becomes large; i.e., the true response amplitude, represented by the PETROS 3.5 solution, has a significantly greater value than that of the linear series analysis. The cause for this behavior can be related to the mean component of the external pressure shown in Figure 15. Whereas the PETROS 3.5 code correctly takes account of the transient membrane stresses induced by this portion of the external load the analytical model can only represent the effect of a static internal pressurization. To show that this is the correct explanation for the deviation between the two curves labeled $p_i = 0$ in Figure 22, the series solution was re-run using $p_i = -0.115$ MPa (- 16.7 psi). The resulting curve (so labeled) may be seen to be in much better agreement with the PETROS 3.5

calculation*. Of course, in the case of large internal pressurization neglect of the mean external pressure is of no consequence.

The effect of varying the blast wave intensity on deflection response has been studied for the bare motor case with no internal pressurization. The results for the maximum deflection (occurring at $\theta = 0$) versus the peak reflected pressure** are presented in Figure 23. The solid curve is based on PETROS 3.5 calculations in which the motor case material was required to remain elastic. The analogous response for the material of Figure 2 is shown by the short-dashed curve, the point surrounded by a triangle corresponding to the "without propellant" curve of Figure 5. The point surrounded by a square represents the series solution for p_r = 207 kPa (30 psi) and $p_i = 0$. It may be seen that the solid curve is tangent to the straight line*** connecting this point to the origin for small $p_{e_{max}}$. Of course, as noted in the previous paragraph, the series solution can be modified to give a maximum deflection in close agreement with the elastic PETROS 3.5 result by use of an "effective" p_i equal to the negative of the mean external pressure. However, the more rigorous PETROS 3.5 calculation is to be preferred.

VI. CONCLUDING REMARKS

The foregoing analysis of solid propellant rocket motor response to air blast loading was restricted to the plane strain case partly to conform to present design practice and also because it was desired to proceed in an evolutionary manner. While this restriction limits the

---

*This discussion is only intended to identify the source of the dominant nonlinear effect. For satisfactory quantitative results the PETROS 3.5 code should be used.

**The blast wave cannot be defined by a single parameter. The parameters p_s, U, β were determined for a selected p_r to correspond to the blast from a one kiloton nuclear device.

***It is not contended that the series solution predicts that the maximum deflection is a strictly linear function of $p_{e_{max}}$. However, since the peak deflection occurs at times $< < 1/\lambda$ and λ varies slowly with $p_{e_{max}}$ the response predicted by the series solution should be nearly linear in $p_{e_{max}}$.

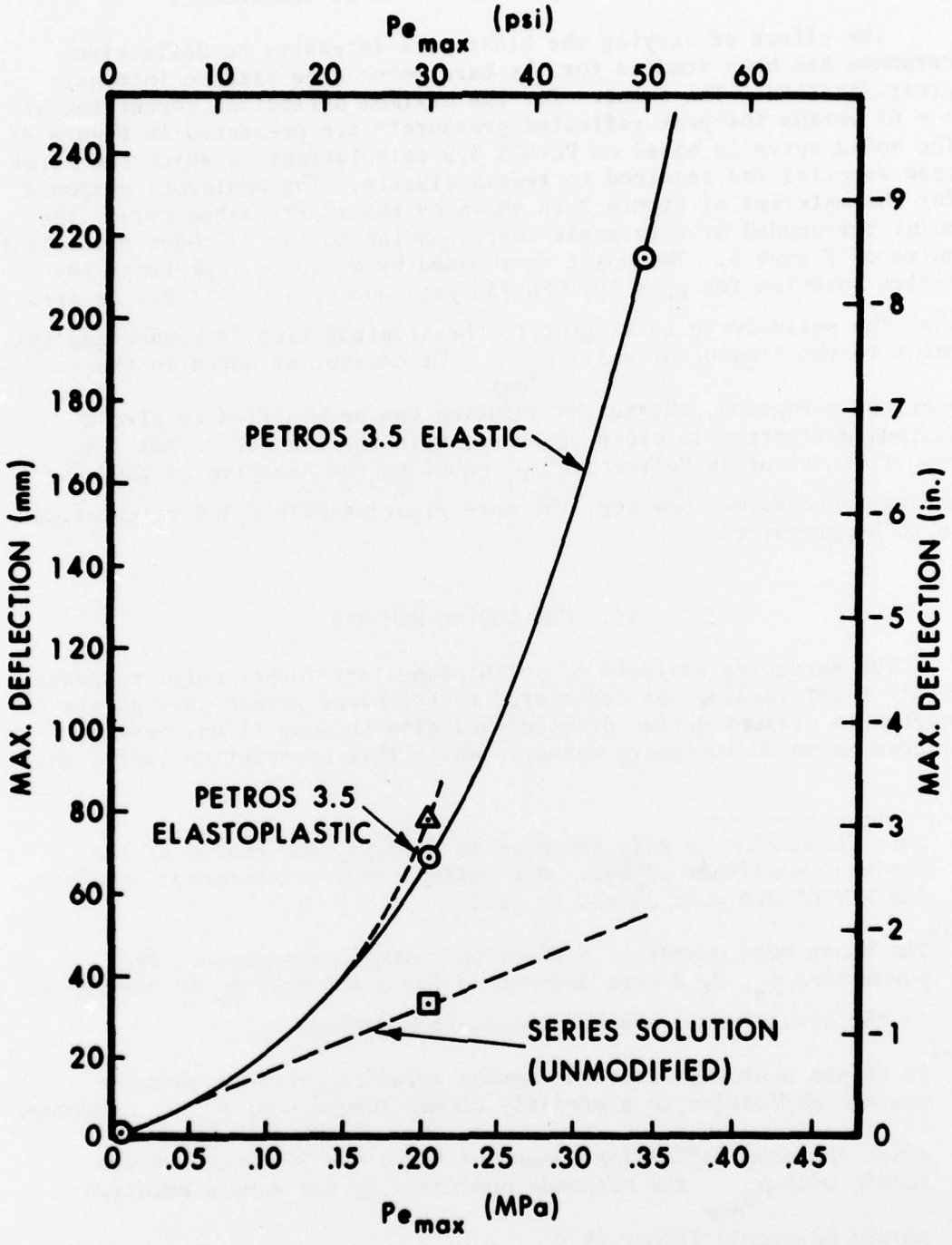

Figure 23. Deflection vs Blast Wave Intensity for $p_i = 0$

applicability of its results to long slender motors the failure mechanisms revealed will certainly have to be considered when more general, three-dimensional analyses are performed.

The finite amplitude elastoplastic shell response code PETROS 3.5, while not capable of fully representing the response of a rocket motor containing propellant, has provided useful baseline data for evaluating predictions derived with other models. The linearized analytical model provides insight into the meaning of the results of the nonlinear numerical analysis even where certain assumptions made in its derivation are violated; e.g., the large amplitude response of the unpressurized motor when the blast loading approaches the critical buckling load. In addition to providing an independent check on the validity of the PETROS 3.5 solution, the modal series solution is preferred for long term response both for economy and because it does not entail the progressive discretization error of the time-marching numerical analysis. Of course, it is appreciated that neither of these approaches models the dissipative mechanisms which are present in physical rocket motor structures but they can certainly provide an upper bound to the response parameters.

The response of a typical rocket motor configuration was calculated for the limiting situations of the bare motor case and of the motor case containing the complete propellant grain, each with no internal pressurization and with the pressurization resulting from propellant combustion. It was found that the unpressurized motors had a much larger deformation than the pressurized motors. Also, for the motors containing propellant it was possible to obtain an estimate of the tensile stress to which the propellant/case bond would be subjected.

The most significant result is the quantification of the greater vulnerability of rocket motors prior to their ignition, whether on the launcher or as upper stages of in-flight missiles. Consideration should be given to the possibility of enhancing the survivability of rocket motors when introduced to a potential nuclear battlefield area by providing a pre-pressurization sufficient to avoid the large amplitude response to air blast characteristic of unpressurized motors.

The combination of the PETROS 3.5 and modal series methodologies provides the designer with a useful approach for assessing the structural integrity of proposed or existing rocket motor configurations when exposed to a hostile load environment. Several extensions of the work reported herein are clearly desirable. The finite element modeling of the viscoelastic propellant grain presently under development will provide the designer with required information concerning critical stresses both within the grain and at the propellant-case interface. A three-dimensional analysis model is also needed, especially for the shorter rocket motors. For an adequate vulnerability assessment of rocket propulsion systems in the presence of nuclear detonations an analysis including the nuclear thermal flux deposition properly time-phased with the air blast arrival must be considered.

REFERENCES

1. J. J. Brisbane, "Advances in Stress Analysis of Solid Propellant Rocket Grains", Rohm and Haas Company Technical Report S-268, Contract DAAH01-70-C-0152, September 1970.

2. R. S. Dunham, "Dynamic Analysis of One Dimensional Thermorheologically Simple Viscoelastic Solids With Nonlinear Heat Conduction Analysis", U.S. Army Missile Command Report No. RK-TR-70-13, July 1970.

3. J. Case et al, "The KNISH/AMGO Photon Energy Deposition and Viscoelastic Material Response Computer Program", Physics International Company, PITR-307-3, August 1972.

4. T. L. Cost and G. E. Weeks, "Automated Evaluation of Interceptor Rocket Motor Designs Under Combined Operational and Nuclear Effects Loads", University of Alabama BER Report No. 176-97, July 1974.

5. S. D. Pirotin, B. A. Berg, and E. A. Witmer, "PETROS 3.5: New Developments and Program Manual for the Finite-Difference Calculation of Large Elastic-Plastic Transient Deformations of Multilayer Variable-Thickness Shells", U.S. Army Ballistic Research Laboratories Contract Report No. 211, February 1975. (AD #A007215)

6. L. Marino, J. W. Leech, and E. A. Witmer, "PETROS 2: A New Finite-Difference Method and Program for the Calculation of Large Elastic-Plastic Dynamically-Induced Deformations of General Thin Shells", U.S. Army Ballistic Research Laboratories Contract Report No. 12, December 1969. (AD #708773)

7. S. Glasstone (Editor), "The Effects of Nuclear Weapons", United States Atomic Energy Commission, April 1962.

8. A. E. H. Love, "A Treatise on the Mathematical Theory of Elasticity", Fourth Edition, Dover Publications, 1944, p. 454.

9. W. Flügge, "Stresses in Shells", Second Edition, Springer-Verlag, 1973, p. 448, 459-460.

10. J. W. Cooley and J. W. Tukey, "An Algorithm for the Machine Calculation of Complex Fourier Series", Mathematical Computations, vol. 19 (1965), pp. 297-301.

11. N. M. Brenner, "Three FORTRAN Programs that Perform the Cooley-Tukey Fourier Transform", Lincoln Laboratory, M.I.T., Technical Note 1967-2.

LIST OF SYMBOLS

$C^m_{n,s}$	Integral defined by Equation (25)
E	Young's modulus
M_θ	Circumferential bending moment/unit length
R	Outside radius of motor case
$S^m_{n,s}$	Integral defined by Equation (26)
U	Shock front velocity
a	Mid-surface radius of motor case
a_o	Sonic velocity at ambient conditions
$f_{n,s}$	Natural frequencies of cylinder
h	Thickness of motor case
j	Summation index
k	$(h/a)^2/12$
m	$t/\Delta t$
n	Circumferential wave number
p_e	External (blast) pressure
p_i	Internal pressure
p_o	Ambient pressure
p_n	Coefficient of n^{th} term of series for p_e
p_r	Reflected peak overpressure
p_s	Side-on overpressure of incident shock
q	$(1-\nu^2)p_i a/(Eh)$
s	Mode family identifier
t	Time
t_a	Time of arrival of shock front
v	Circumferential component of displacement

LIST OF SYMBOLS (Continued)

w	Radial component of displacement
w_n	Amplitude of n^{th} term in series for w
$\Delta C^j_{n,s}$	Integral defined by Equation (23)
$\Delta S^j_{n,s}$	Integral defined by Equation (24)
Δt	Time increment
α	$\frac{12(1-\nu^2)a^4}{Eh^3}$
β	$\frac{Eh}{(1-\nu^2)\rho h a^2}$
$\bar{\varepsilon}_\theta$	Circumferential membrane strain
θ	Circumferential angular coordinate
λ	Blast wave decay coefficient
ν	Poisson's ratio
ρ	Mass density
σ_o	Yield stress
τ	Dummy time variable in convolution integrals
$\tau_{n,s}$	Period of the (n,s) mode
$\omega_{n,s}$	Circular frequency of (n,s) mode

DISTRIBUTION LIST

No. of Copies	Organization
12	Commander Defense Documentation Center ATTN: DDC-DDA Cameron Station Alexandria, VA 22314
2	Assistant to the Secretary of Defense (Atomic Energy) ATTN: Document Control Donald R. Cotter Washington, DC 20301
1	Director of Defense Research and Engineering ATTN: Dir/Tech Info Washington, DC 20301
1	Office of Deputy Under Secretary of Defense for Research & Engineering (ET) ATTN: Mr. J. Persh Staff Specialist for Materials and Structures Room 3D1089, The Pentagon Washington, DC 20301
1	Director Defense Advanced Research Projects Agency 1400 Wilson Boulevard Arlington, VA 22209
3	Director Institute for Defense Analyses ATTN: Dr. J. Menkes Dr. J. Bengston Tech Info Ofc 400 Army-Navy Drive Arlington, VA 22202
1	Director Weapons Sys Evaluation Group ATTN: CPT Donald E. McCoy Washington, DC 20305
4	Director Defense Intelligence Agency ATTN: DT-1B DB-4C, E.O. Farrell DT-2, Wpns & Sys Div RDS-3A4 Washington, DC 20301
9	Director Defense Nuclear Agency ATTN: STSI/Archives SPAS/Mr. J. Moulton STSS/Dr. E. Sevin (2 cys) STVL/Dr. La Vier RATN/Mr. Rubenstein DDST/Mr. P. Haas STTL/Tech Lib (2 cys) Washington, DC 20305
2	Commander Field Command, DNA ATTN: FCPR FCTMOF Kirtland AFB, NM 87115
1	Commander Field Command, DNA Livermore Branch ATTN: FCPRL P. O. Box 808 Livermore, CA 94550
1	DNA Information and Analysis Center TEMPO, General Electric Co. Center for Advanced Studies ATTN: DASIAC 816 State Street Santa Barbara, CA 93102
2	Director Defense Civil Preparedness Agency ATTN: Mr. George Sisson/RF-SR Technical Library Washington, DC 20301

DISTRIBUTION LIST

No. of Copies	Organization
1	Director National Security Agency ATTN: E. F. Butala, R15 Fort George G. Meade, MD 20755
3	Director Joint Strategic Target Planning Staff, JCS ATTN: Sci & Tech Info Lib JLTW-2 DOXT Offutt AFB Omaha, NB 68113
2	Chairman Joint Chiefs of Staff ATTN: J-3, Operations J-5, Plans & Policy (R&D Division) Washington, DC 20301
1	Commander US Army Materiel Development and Readiness Command ATTN: DRCDMD-ST, N. Klein 5001 Eisenhower Avenue Alexandria, VA 22333
1	Commander US Army Materiel Development and Readiness Command ATTN: Technical Library 5001 Eisenhower Avenue Alexandria, VA 22333
1	Commander US Army Aviation Research and Development Command ATTN: DRSAV-E P. O. Box 209 St. Louis, MO 63166
1	Director US Army Air Mobility Research and Development Laboratory Ames Research Center Moffett Field, CA 94035
1	Director Lewis Directorate US Army Air Mobility Research and Development Laboratory Lewis Research Center ATTN: Mail Stop 77-5 21000 Brookpark Road Cleveland, OH 44135
2	Commander US Army Electronics Research and Development Command Technical Support Activity ATTN: DELSD-L DRDEL-SA, W.S. McAfee Fort Monmouth, NJ 07703
1	Commander US Army Communications Rsch and Development Command ATTN: DRDCO-PPA-SA Fort Monmouth, NJ 07703
7	Commander US Army Missile Research and Development Command ATTN: DRDMI-R Mr. B. Cobb Mr. W. Thomas Mr. L. Lively Mr. T. H. Duerr Mr. R. Petty DRDMI-YDL Redstone Arsenal, AL 35809

DISTRIBUTION LIST

No. of Copies	Organization
3	Commander US Army Missile Materiel Readiness Command ATTN: DRSMI-Q DRSMI-XS, Ch Scientist Technical Library Redstone Arsenal, AL 35809
3	Commander US Army Missile Materiel Readiness Command ATTN: Lance Project Office Pershing Project Office Hawk Project Office Redstone Arsenal, AL 35809
1	Commander US Army Tank Automotive Research & Development Cmd ATTN: DRDTA-UL Warren, MI 48090
2	Commander US Army Mobility Equipment Research & Development Cmd ATTN: DRDME-RI, Dr. K. Oscar DRDME-NN, Dr. P. Herberlein Fort Belvoir, VA 22060
5	Commander US Army Armament Research and Development Command ATTN: DRDAR-LCN-F Mr. Warren Reiner P. Angelotti (2 cys) DRDAR-TSS (2 cys) Dover, NJ 07801
5	Commander US Army Armament Research and Development Command ATTN: DRDAR-LC, Dr. J. Frasier DRDAR-LCA DRDAR-LCS DRDAR-AC DRDAR-SE Dover, NJ 07801
1	Commander US Army Armament Materiel Readiness Command ATTN: DRSAR-LEP-L, Tech Lib Rock Island, IL 61299
2	Commander US Army Watervliet Arsenal ATTN: DRDAR-LCB-TL Watervliet, NY 12189
7	Commander US Army Harry Diamond Labs ATTN: Mr. James Gaul Mr. L. Belliveau Mr. J. Gwaltney Mr. F. N. Wimenitz Mr. Bill Vault Dr. R. Oswald Mr. J. Rosado 2800 Powder Mill Road Adelphi, MD 20783
4	Commander US Army Materials and Mechanics Research Center ATTN: Technical Library John Mescall Richard Shea Dr. S. C. Chou Watertown, MA 02172

DISTRIBUTION LIST

No. of Copies	Organization
1	Commander US Army Natick Research and Development Command ATTN: DRXRE, Dr. D. Sieling Natick, MA 01762
1	Commander US Army Foreign Science and Technology Center ATTN: Rsch & Concepts Br. 220 Seventh Street, NE Charlottesville, VA 22901
2	Commander US Army Nuclear & Chemical Agency ATTN: ACTA-NAW Technical Library 7500 Backlick Rd, Bldg. 2073 Springfield, VA 22150
1	Commander US Army Training and Doctrine Command ATTN: ATCD-SA, Mr. Oscar Wells Fort Monroe, VA 23651
2	Director US Army TRADOC Systems Analysis Activity ATTN: LTC John Hesse ATAA-SL, Tech Lib White Sands Missile Range NM 88002
1	Commander US Army Combined Arms Combat Developments Activity ATTN: ATCA-CO, L. C. Pleger Fort Leavenworth, KS 66027
1	Interservice Nuclear Weapons School ATTN: Technical Library Kirtland AFB, NM 87115
1	Deputy Assistant Secretary of the Army (R&D) ATTN: Asst for Rsch Washington, DC 20310
2	Deputy Chief of Staff for Operations & Plans ATTN: Technical Library Dir of Chemical and Nuclear Operations Department of the Army Washington, DC 20310
2	HQDA (DAMA-AR; NCL Div) Washington, DC 20310
2	Commander US Army Engineer Waterways Experiment Station ATTN: Library, Mr. W. Flateau P. O. Box 631 Vicksburg, MS 39180
3	Director US Army BMD Advanced Technology Center ATTN: CRDABH-X CRDABH-S M. Whitfield Huntsville, AL 35807
2	Commander US Army BMD Systems Command ATTN: BMDSC-TFN, N.J. Hurst J. Veeneman P. O. Box 1500 Huntsville, AL 35807
1	Program Manager US Army BMD Program Office ATTN: John Shea 5001 Eisenhower Avenue Alexandria, VA 22333

DISTRIBUTION LIST

No. of Copies	Organization
3	Commander US Army Research Office ATTN: Dr. E. A. Saibel Dr. G. Mayer Dr. J. Chandra P. O. Box 12211 Research Triangle Park NC 27709
1	Commander US Army Europe ATTN: AEAGB (S&E) APO New York 09403
1	Assistant Secretary of the Navy (Research & Development) Navy Department Washington, DC 20350
1	Chief of Naval Material ATTN: MAT 0323 Department of the Navy Arlington, VA 22217
1	Chief of Naval Research ATTN: N. Perrone Department of the Navy Washington, DC 20360
1	Commander Naval Air Systems Command ATTN: AIR-532 Washington, DC 20361
2	Commander Naval Sea Systems Command ATTN: ORD-91313 Library Code 03511 Department of the Navy Washington, DC 20362
1	Director Strategic Systems Projects Ofc ATTN: NSP-43, Tech Lib Department of the Navy Washington, DC 20360
1	Commander David W. Taylor Naval Ship Research & Development Ctr ATTN: Lib Div, Code 522 Bethesda, MD 20084
2	Commander Naval Surface Weapons Center ATTN: Library Br., DX-21 Dr. W. Soper Dahlgren, VA 22448
3	Commander Naval Surface Weapons Center ATTN: Code WA501/Navy Nuclear Programs Office Code WX21/Tech Lib Code 240/J. Petes Silver Spring, MD 20910
2	Commander Naval Weapons Center ATTN: Code 533, Tech Lib Code 6031, Dr.W.Stronge China Lake, CA 93555
1	Commander Naval Weapons Eval. Facility ATTN: Document Control Kirtland AFB Albuquerque, NM 87117
3	Officer-in-Charge Civil Engineering Laboratory Naval Construction Btn Ctr ATTN: Dr. W. A. Shaw John Crawford Technical Library Port Hueneme, CA 93041
1	Commander Naval Research Laboratory ATTN: Code 2027, Tech Lib Washington, DC 20375

DISTRIBUTION LIST

No. of Copies	Organization
2	Superintendent Naval Postgraudate School ATTN: Tech Reports Sec. Code 57, Prof. R. Ball Monterey, CA 93940
2	AFATL (DLYV, P. Nash) Eglin AFB, FL 32542
4	AFWL (WLTL; DYT, MAJ G. Ganong; DYT, Mr. Charles Needham; DUT, CPT D. Marten) Kirtland AFB, NM 87117
2	Commander-in-Chief Strategic Air Command ATTN: NRI-STINFO Lib XPFS Offutt AFB, NM 68113
2	AFFDL (FDTR, Dr. F.J. Janik, Jr.; FBE, Mr. R.M. Bader) Wright-Patterson AFB, OH 45433
1	AFML (LLN, Dr. T. Nicholas) Wright-Patterson AFB, OH 45433
1	Headquarters Energy Research and Development Administration Dept of Military Applications Washington, DC 20545
1	US Energy Research and Development Administration Division of Headquarters Svc ATTN: Doc Control for Classified Tech Lib Library Branch G-043 Washington, DC 20545
1	US Energy Research and Development Administration Albuquerque Operations Office ATTN: Doc Control for Tech Lib P. O. Box 5400 Albuquerque, NM 87115
1	Director Lawrence Livermore Laboratory ATTN: Docu Control for Tech Lib P. O. Box 969 Livermore, CA 94550
1	Director Lawrence Livermore Laboratory Technical Information Div P. O. Box 808 Livermore, CA 94550
2	Director Los Alamos Scientific Lab ATTN: Docu Control P. O. Box 1663 Los Alamos, NM 87544
1	Director National Aeronautics and Space Administration Lewis Research Center Cleveland, OH 44135
1	Director National Aeronautics and Space Administration Marshall Space Flight Center Huntsville, AL 35812
1	Director NASA Scientific and Technical Information Facility P. O. Box 8757 Baltimore/Washington International Airport, MD 21240

DISTRIBUTION LIST

No. of Copies	Organization
1	National Academy of Sciences ATTN: Mr. D. G. Groves 2101 Constitution Avenue, NW Washington, DC 20418
1	Aeronautical Research Assoc. of Princeton, Inc. ATTN: Dr. C. Donaldson 50 Washington Road Princeton, NJ 08540
1	Aerospace Corporation ATTN: Tech Info Svcs P. O. Box 92957 Los Angeles, CA 90009
1	Agbabian Associates ATTN: M. Agbabian 250 North Nash Street El Segundo, CA 90245
1	AVCO ATTN: Res Lib A830, Rm 7201 201 Lowell Street Wilminton, MA 01887
2	Battelle Columbus Laboratories ATTN: Dr. L. E. Hulbert Mr. J. E. Backofen, Jr. 505 King Avenue Columbus, OH 43201
1	The BDM Corporation ATTN: Richard Hensley P. O. Box 9274 Albuquerque International Albuquerque, NM 87119
2	The Boeing Company ATTN: Aerospace Library R. H. Carlson P. O. Box 3707 Seattle, WA 98124
1	Brown Engineering Co., Inc. ATTN: Manu Patel Cummings Research Park Huntsville, AL 35807
1	California Research and Technology, Inc. ATTN: Technical Library 6269 Variel Avenue Woodland Hills, CA 91364
1	Civil/Nuclear Systems Corp. ATTN: Robert Crawford 1200 University NE Albuquerque, NM 87102
1	General Electric Company-TEMPO 7800 Marble NE Albuquerque, NM 87110
1	J. G. Engineering Research Associates 3831 Menlo Drive Baltimore, MD 21215
2	Kaman Avidyne ATTN: Dr. N. P. Hobbs Mr. S. Criscione 83 Second Avenue Northwest Industrial Park Burlington, MA 01830
3	Kaman Science Corporation ATTN: Dr. F. H. Shelton Dr. D. Sachs Dr. R. Keefe 1500 Garden of the Gods Road Colorado Springs, CO 80907
1	Lockheed Missiles & Space Co. ATTN: Technical Library P. O. Box 504 Sunnyvale, CA 94088

DISTRIBUTION LIST

No. of Copies	Organization
1	Martin Marietta Aerospace Orlando Division P. O. Box 5837 Orlando, FL 32805
1	McDonnell Douglas Astronautics Corporation 5301 Bolsa Avenue Huntington Beach, CA 92647
1	Merritt Cases, Inc. ATTN: Technical Library P. O. Box 1206 Redlands, CA 92373
1	The Mitre Corporation ATTN: Library P. O. Box 208 Bedford, MA 01730
1	Physics International Corp 2700 Merced Street San Leandro, CA 94577
4	R&D Associates ATTN: Dr. H. L. Brode Jerry Carpenter J. G. Lewis Technical Library P. O. Box 9695 Marina del Rey, CA 90291
1	The Rand Corporation 1700 Main Street Santa Monica, CA 90406
2	Sandia Laboratories ATTN: Info Distr Division Dr. W. A. von Riesemann Albuquerque, NM 87115
1	Science Applications, Inc. ATTN: Technical Library P. O. Box 3507 Albuquerque, NM 87110
2	Science Applications, Inc. ATTN: Technical Library P. O. Box 3507 Albuquerque, NM 87110
2	Science Applications, Inc. ATTN: R. Seebaugh John Mansfield 1651 Old Meadow Road McLean, VA 22101
1	Science Applications, Inc. [illegible]0 Washington Ave, Suite 120 San Leandro, CA 94577
2	Science Applications, Inc. ATTN: Technical Library Michael McKay P. O. Box 2351 La Jolla, CA 92038
1	TRW Systems Group ATTN: Greg Hulcher San Bernardino Operations P. O. Box 1310 San Bernardino, CA 92402
1	TRW Systems Group ATTN: Tech Info Ctr/S-1930 One Space Park Redondo Beach, CA 92078
1	Weidlinger Assoc. Consulting Engineers ATTN: M. L. Baron 110 East 59th Street New York, NY 10022

DISTRIBUTION LIST

No. of Copies	Organization
2	Denver Research Institute University of Denver ATTN: Mr. J. Wisotski Technical Library P. O. Box 10127 Denver, CO 80210
1	Florida Atlantic University Dept of Ocean Engineering ATTN: Prof. K. K. Stevens Boca Raton, FL 33432
1	IIT Research Institute ATTN: Technical Library 10 West 35th Street Chicago, IL 60616
1	Massachusetts Institute of Technology Aeroelastic and Structures Research Laboratory ATTN: Dr. E. A. Witmer Cambridge, MA 02139
2	Southwest Research Institute ATTN: Dr. H. N. Abramson Dr. W. E. Baker 8500 Culebra Road San Antonio, TX 78228
2	Stanford Research Institute ATTN: Dr. Herbert E. Lindberg Dr. G. R. Abrahamson 333 Ravenswood Avenue Menlo Park, CA 94025
1	Texas A&M University Dept of Aerospace Engineering ATTN: Dr. Walter E. Haisler College Station, TX 77843
1	University of Alabama ATTN: Dr. T. L. Cost P. O. Box 2908 University, AL 35486
1	University of Delaware Department of Mechanical and Aerospace Engineering ATTN: Prof. J. R. Vinson Newark, DE 19711
	Aberdeen Proving Ground Dir, USAMSAA ATTN: Dr. J. Sperrazza Mr. R. Norman, GWD DRXSY-GS DRXSY-RE DRXSY-MP, H. Cohen Cdr, USATECOM ATTN: DRSTE-DA DRSTE-SG-H